J. Fluid Mech. (2014), vol. 748, pp. 36–84.
doi:10.1017/jfm.2014.147

Effect of mean and fluctuating pressure gradients on boundary layer turbulence

Pranav Joshi, Xiaofeng Liu and Joseph Katz†

Department of Mechanical Engineering, Johns Hopkins University, Baltimore, MD 21218, USA

(Received 15 April 2013; revised 31 January 2014; accepted 12 March 2014; first published online 28 April 2014)

This study focuses on the effects of mean (favourable) and large-scale fluctuating pressure gradients on boundary layer turbulence. Two-dimensional (2D) particle image velocimetry (PIV) measurements, some of which are time-resolved, have been performed upstream of and within a sink flow for two inlet Reynolds numbers, $Re_\theta(x_1) = 3360$ and 5285. The corresponding acceleration parameters, K, are 1.3×10^{-6} and 0.6×10^{-6}. The time-resolved data at $Re_\theta(x_1) = 3360$ enables us to calculate the instantaneous pressure distributions by integrating the planar projection of the fluid material acceleration. As expected, all the locally normalized Reynolds stresses in the favourable pressure gradient (FPG) boundary layer are lower than those in the zero pressure gradient (ZPG) domain. However, the un-scaled stresses in the FPG region increase close to the wall and decay in the outer layer, indicating slow diffusion of near-wall turbulence into the outer region. Indeed, newly generated vortical structures remain confined to the near-wall region. An approximate analysis shows that this trend is caused by higher values of the streamwise and wall-normal gradients of mean streamwise velocity, combined with a slightly weaker strength of vortices in the FPG region. In both boundary layers, adverse pressure gradient fluctuations are mostly associated with sweeps, as the fluid approaching the wall decelerates. Conversely, FPG fluctuations are more likely to accompany ejections. In the ZPG boundary layer, loss of momentum near the wall during periods of strong large-scale adverse pressure gradient fluctuations and sweeps causes a phenomenon resembling local 3D flow separation. It is followed by a growing region of ejection. The flow deceleration before separation causes elevated near-wall small-scale turbulence, while high wall-normal momentum transfer occurs in the ejection region underneath the sweeps. In the FPG boundary layer, the instantaneous near-wall large-scale pressure gradient rarely becomes positive, as the pressure gradient fluctuations are weaker than the mean FPG. As a result, the separation-like phenomenon is markedly less pronounced and the sweeps do not show elevated small-scale turbulence and momentum transfer underneath them. In both boundary layers, periods of acceleration accompanying large-scale ejections involve near-wall spanwise contraction, and a high wall-normal momentum flux at all elevations. In the ZPG boundary layer, although some of the ejections are preceded, and presumably initiated, by regions of adverse pressure gradients and sweeps upstream, others are not. Conversely, in the FPG boundary layer, there is no evidence of sweeps or adverse pressure gradients immediately upstream of ejections. Apparently, the mechanisms initiating these ejections are either different from those involving large-scale sweeps or occur far upstream of the peak in FPG fluctuations.

Key words: boundary layers, boundary layer structure, turbulent boundary layers

---

† Email address for correspondence: katz@jhu.edu

1. Introduction

Turbulent boundary layers are subjected to mean favourable pressure gradients (FPG) in numerous applications, and hence have been studied extensively. However, some aspects of their physics, especially the interaction between the large-scale structures and the near-wall turbulence, have rarely been investigated. Such interactions have been shown to become increasingly important in zero pressure gradient (ZPG) boundary layers with increasing Reynolds numbers (Marusic *et al.* 2010). Among the many potential contributors, the role played by large-scale pressure gradient fluctuations in modulating the near-wall turbulence has hardly been explored. In addition to possibly modifying near-wall turbulence production, pressure gradient fluctuations also play an important role in the transfer of energy among different components of the Reynolds stress through the so-called pressure strain correlations. Until recently, experimental studies involving the pressure away from boundaries have been very limited (details follow), primarily due to the difficulty in performing non-intrusive free-stream pressure measurements. To this end, we perform particle image velocimetry (PIV)-based, simultaneous measurements of pressure and velocity in both ZPG and FPG boundary layers. The analysis that follows investigates the effect of large-scale pressure gradient fluctuations on the structure of turbulence of both boundary layers.

Various coherent structures intimately connected with the production of near-wall turbulence and its transport into the outer layer, such as hairpin and streamwise vortices, and low-speed streaks have been described in numerous previous studies, too many to summarize here (e.g. Robinson 1991; Panton 2001; Adrian 2007). Several mechanisms for the generation of these structures have been proposed. For example, Zhou *et al.* (1999) describe the generation of secondary and tertiary hairpin vortices from the primary vortex by formation of self-induced kinks and subsequent reconnection of vortex elements. Smith *et al.* (1991) show that 'offspring' vortices can be generated as a result of the 'viscous-inviscid' interaction of the parent vortex with the wall, and that low-speed streaks do not play an active role in this process. Conversely, Jiménez & Pinelli (1999) and Schoppa & Hussain (2002) show, using direct numerical simulation (DNS) data, that the instability of the low-speed streaks is the dominant mechanism for the generation of streamwise vortices in the near-wall region. Although the details in these two studies differ, both suggest that the formation of streamwise vortices is largely independent of the outer flow. Using high-resolution digital holographic PIV, Sheng, Malkiel & Katz (2009) show that hairpin vortices and the associated low-speed streaks are formed by abrupt lifting of vortex lines very close to the wall. The cause of this lifting, however, is not known.

Although the evidence for self-sustained near-wall turbulence generation independent of the outer flow is strong, it has also been established that the large-scale outer layer structures modulate the near-wall turbulence (Hutchins & Marusic 2007). Indeed, Mathis, Hutchins & Marusic (2009) show that the small-scale turbulence in the buffer layer is higher underneath high-momentum regions in the outer layer. Chung & McKeon (2010) and Hutchins *et al.* (2011) demonstrate that there is a phase delay between the large- and small-scale velocity fluctuations, and that the latter tend to be higher in regions of adverse streamwise gradients of large-scale fluctuations. Ganapathisubramani *et al.* (2012) suggest that this phase difference could be caused by differences in convection velocities of the large- and small-scale structures. For very-high-Reynolds-number boundary layers, Hunt & Morrison (2000) propose a 'top-down' model, in which outer layer, large-scale eddies impinge on the wall, generating high Reynolds shear stress and small-scale turbulence. The DNS results of Toh & Itano (2005) also suggest that large-scale outer layer structures play an active role in the near-wall generation and dynamics of small-scale turbulence. Numerous studies have focused on very large structures, also called 'superstructures' (Hutchins & Marusic 2007), in the logarithmic and wake regions of boundary layers (e.g. Tomkins & Adrian 2003; Ganapathisubramani *et al.* 2005; Hutchins & Marusic 2007; Hutchins *et al.* 2011) and pipe flows (Kim & Adrian 1999; Bailey & Smits 2010). These superstructures involve regions of momentum deficit or surplus with substantial streamwise extent. Some studies suggest that these structures are formed by streamwise alignment of hairpin packets (e.g. Kim & Adrian 1999; Balakumar & Adrian 2007). Others suggest that they are the most amplified instability modes of the mean velocity profile (Del Álamo & Jiménez 2006), or observe that they are formed by the collective behaviour of the small-scale structures (Toh & Itano 2005).

Systematic studies of the impact of large-scale pressure gradient fluctuations have been rare. Using large eddy simulations (LES) for a channel flow, Kim (1983, 1985) shows that streamwise adverse pressure gradients occurring within sweeping events, with scales of several hundred wall units, cause ejections downstream, in a phenomenon resembling flow separation. As will be discussed later, the present results, although at significantly larger scales, are in agreement with these findings. At smaller scales, DNS of Johansson, Alfredsson & Kim (1991) and LES of Lo, Voke & Rockliff (2000) show that the pressure fluctuations peak in the vicinity of inclined internal shear layers in the buffer layer. Moin & Kim (1982) and Lenaers *et al.* (2012) observe regions of elevated pressure around high-momentum fluid in the inner layer, which they attribute to 'quasi-stagnation' regions formed by splatting fluid. Using DNS, Kim (1989) reports that while the instantaneous $\partial p/\partial y$ and $\partial p/\partial z$ contours at the wall are elongated in the streamwise direction, those of $\partial p/\partial x$ are not. Here, p is the pressure and x, y and z are, respectively, the streamwise, wall-normal and spanwise directions. Furthermore, two-point pressure correlation contours are aligned normal to the wall, unlike those of the velocity, which are inclined to the wall. Space–time correlations are used by Choi & Moin (1990) to show that large-scale pressure fluctuation events travel faster than small-scale events. Moin & Kim (1982) and Spalart (1988) compute the contribution of pressure terms in the Reynolds stress budgets, and pressure fluctuations spectra are discussed in Choi & Moin (1990) and Jiménez & Hoyas (2008).

Until recently, experimental studies of pressure fluctuations in boundary layers have been limited to intrusive point measurements away from the wall (e.g. Elliott 1972; Schols & Wartena 1986; Tsuji *et al.* 2007), and to applications of surface-mounted probes (e.g. Willmarth & Wooldridge 1962; Bull 1967; Wills 1970; Thomas & Bull 1983; Morrison & Bradshaw 1991). Bull (1967) and Wills (1970) report a convection velocity increasing with scale, in agreement with Choi & Moin (1990). According to Tsuji *et al.* (2007), there is a positive two-point correlation between the pressure at the wall and at other elevations, but for regions with limited streamwise extent. Elliott (1972) finds that large-scale velocity and pressure fluctuations in the logarithmic region of the atmospheric boundary layer are approximately in phase. Estimating the streamwise pressure gradients based on a single point measurement in the log layer and invoking Taylor's hypothesis, Schols & Wartena (1986) report that the fluctuating pressure gradients are positive (adverse) during periods of high momentum. Following the same approach, but relying on wall measurements, Thomas & Bull (1983), Kobashi & Ichijo (1986) and Morrison & Bradshaw (1991) show that sweeps are accompanied by adverse pressure gradients and are followed downstream by ejections and FPG. Furthermore, Thomas & Bull (1983) report that the small-scale pressure fluctuations are relatively high during periods of large-scale adverse pressure gradients. Recently, several studies have examined the fluid acceleration in boundary layers based on PIV data. Christensen & Adrian (2002) use time-resolved PIV in a turbulent channel flow to show that the temporal acceleration term dominates the so-called 'bulk convective acceleration', i.e. $\partial u_i/\partial t + U_b \partial u_i/\partial x$. Here, u_i is the velocity component in the 'ith' direction, t is time, and U_b is the wall-normal averaged mean streamwise velocity. This observation implies that small vortices remain nearly frozen in time. Employing tomographic PIV data to calculate the instantaneous pressure fields in a turbulent boundary layer by integrating the Poisson equation, Ghaemi, Ragni & Scarano (2012) report good agreement between their results and point wall pressure measurement.

The effects of favourable mean pressure gradients on the structure of turbulent boundary layers, one of the present foci, have been studied extensively (e.g. Blackwelder & Kovasznay 1972; Escudier *et al.* 1998; Fernholz & Warnack 1998; Bourassa & Thomas 2009). The strength of the imposed FPG is typically expressed in terms of the acceleration parameter, K, or the pressure gradient parameter, K_p, defined as,

$$K = \frac{\nu}{U_0^2}\frac{\mathrm{d}U_0}{\mathrm{d}x}, \quad K_p = \frac{\nu}{\rho u_\tau^3}\frac{\mathrm{d}P}{\mathrm{d}x}. \tag{1.1a,b}$$

Here $U_0(x)$ is the mean freestream velocity, $u_\tau(x)$ is the friction velocity, $P(x)$ is the mean pressure, ρ is the density and ν is the kinematic viscosity of the fluid. As summarized by Sreenivasan (1982), relaminarization may occur if $K > \sim 3 \times 10^{-6}$ (Spalart 1986) is maintained over a sufficient streamwise distance. Even under moderate acceleration ($K < \sim 2.5 \times 10^{-6}$), the Reynolds stress distribution in the so-called 'laminarescent' boundary layer is altered significantly. If K is constant, e.g. in a sink flow, or changes gradually, laminarescent boundary layers can attain an equilibrium state, i.e. the appropriately non-dimensionalized mean velocity and Reynolds stress profiles are invariant in the streamwise direction (Townsend 1976). For such moderate K, the shape factor decreases, the skin friction coefficient increases, and the mean velocity profile has a logarithmic region, but κ, the Kármán constant, increases with K (Dixit & Ramesh 2008; Bourassa & Thomas 2009). As the flow accelerates, but before reaching equilibrium, the absolute magnitudes of all Reynolds stress components increase axially close to the wall. However, they decrease when scaled with the local freestream velocity. As for the outer region, published trends differ, with some reporting little change or an increase (Jones & Launder 1972; Piomelli, Balaras & Pascarelli 2000), while others observe a decrease (Escudier *et al.* 1998; Fernholz & Warnack 1998) in stresses.

Unlike the wealth of information about coherent structures in ZPG boundary layers, relatively few studies have investigated them in FPG boundary layers. Piomelli *et al.* (2000) use LES to show that the low-speed streaks in the buffer and log layers become more elongated with fewer 'wiggles'. The vortical structures extend to smaller distances away from the wall and their inclination angles decrease. Jang, Sung & Krogstad (2011) use DNS to reveal that the streamwise velocity correlation contours are aligned at shallower angles with the wall, while measurements of Dixit & Ramesh (2010) show that these inclination angles decrease systematically as K increases. For very mild FPG ($K \sim 0.08 \times 10^{-6}$), Harun *et al.* (2013) find that the outer-layer large-scale structures are weaker than those in ZPG boundary layers. In DNS results at $K = 2.5 \times 10^{-6}$, Spalart (1986) observes large patches of quiescent fluid, accompanied locally by low wall shear stress and wide normalized (in wall units) spacing of the buffer layer low-speed streaks. These patches are not observed at $K = 1.5 \times 10^{-6}$. The increase in the streak spacing only for large K is consistent with other studies (Kline *et al.* 1967; Talamelli *et al.* 2002; Pearce, Denissenko & Lockerby 2013). The normalized frequency of bursting, believed to be intimately connected with turbulence production, also decreases under strong FPG (Kline *et al.* 1967; Ichimiya, Nakamura & Yamashita 1998).

In all of the above-mentioned studies, very little information is provided about the possible role played by large-scale pressure gradient fluctuation events on the flow structure and turbulence in ZPG and FPG boundary layers. To address this question, we use time-resolved PIV data to calculate the in-plane distribution of material acceleration, and then spatially integrate it to calculate the instantaneous pressure distributions (Liu & Katz 2006). The effect of the missing out-of-plane component is also evaluated. Section 2 describes the experimental set-up, as well as measurement and data analysis procedures. Mean flow and turbulence statistics are discussed in § 3. The greatly reduced wall-normal transport of coherent structures in the FPG boundary layer is discussed in § 4, and two-point correlations involving pressure and velocity are presented in § 5. In § 6, we show that the separation-like phenomenon caused by the adverse pressure gradient fluctuations accompanying large-scale sweeps in the ZPG boundary layer is greatly suppressed in the FPG domain. Furthermore, we demonstrate that, in both boundary layers, the impact of large-scale pressure gradient fluctuations on the flow structure is very different from that of mean pressure gradients.

2. Experimental set-up and measurement procedures

2.1. *Facility and data acquisition*

Experiments have been performed in a rectangular channel, which is a part of the optically index-matched flow facility at Johns Hopkins University described in Hong, Katz & Schultz (2011), Wu, Miorini & Katz (2011), Hong *et al.* (2012) and Talapatra & Katz (2012, 2013). Figure 1 shows the schematic of the relevant section of the facility. The channel walls are made of acrylic and the liquid is a solution of NaI in water (62 % by weight, $\rho = 1800$ kg m^{-3}, $\nu = 1.1 \times 10^{-6}$ m^2 s^{-1}), whose refractive index is very close to that of acrylic. The index matching minimizes reflection at the surfaces, and enables near-wall optical measurements. The settling chamber before the channel entrance contains a honeycomb (A) and two screens as flow straighteners. It is followed by a 4:1, 2D contraction. A second honeycomb (B) with 3.4 mm cells is introduced at the entrance and a 2 mm thick mesh is attached to the lower wall to improve the spanwise uniformity of the flow. The channel is 51 mm high and 203 mm wide. To generate a sink flow, the top wall transitions smoothly to an inclined surface starting from 775 mm downstream of honeycomb B, which decreases the channel height to 27 mm over a streamwise distance of $l = 313$ mm. The origin of the coordinate system is located on the lower wall, at the beginning of the accelerating region. In the following discussion, u, v, w represent instantaneous velocities, while U, V, and W are the corresponding mean values along the x, y and z directions, respectively. Fluctuations are indicated by $(\,)'$, and ensemble averaged quantities by $\langle\,\rangle$. Measurements are performed in the boundary layers on the lower wall and the first site ($x_1/l = -0.04$) is located 762 mm downstream of honeycomb B.

We perform PIV measurements at inlet Reynolds numbers, $Re_\theta(x_1) = \theta(x_1)U_0(x_1)/\nu = 5285$ and 3360, where θ is the momentum thickness of the boundary layer (Pope 2000). The ZPG conditions are represented by results obtained at x_1. Although the flow there begins to accelerate, K is still very low. For $Re_\theta(x_1) = 5285$,

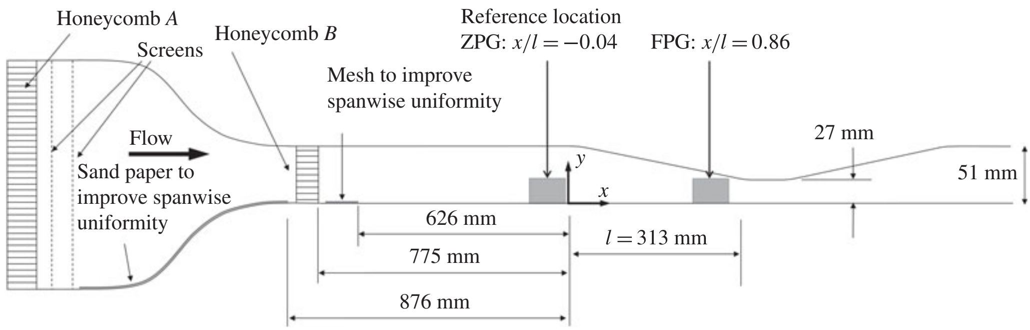

FIGURE 1. Schematic of the experimental set-up.

statistically independent x–y plane data is recorded at eight locations, x_k, as listed in table 1, with the last site representing the FPG boundary layer. The flow is seeded with 1–6 μm diameter silver-coated glass spheres (mean diameter $d_p \sim 2$ μm, density $\rho_p = 2600$ kg m^{-3}), and illuminated with a ∼1 mm thick Nd:YAG (532 nm) laser sheet. The difference between particle and fluid densities has negligible effect on the measurements, as the Stokes number, $St = \tau_p/\tau_f$, is less than 0.04, where $\tau_p = \rho_p d_p^2/18\rho\nu$ is the particle relaxation time, and $\tau_f = \nu/u_\tau^2$ is the characteristic smallest flow time scale (Raffel *et al.* 2007). Images are recorded using a 4864 × 3248 pixels^2 CCD camera (pixel pitch 7.4 μm). They are enhanced by using a modified histogram equalization procedure, and velocity is calculated using an in-house-developed correlation-based program (Roth & Katz 2001). The interrogation window size (Δ) is 32 × 32 pixels^2, with 50 % overlap between windows. At least 5000 velocity distributions are used to obtain flow statistics. In order to cover the entire boundary layer, four different magnifications are used, as summarized in table 1.

For $Re_\theta(x_1) = 3360$, time-resolved measurements are performed in x–y planes around $x/l = -0.04$ and 0.86, and in x–z planes at $y = 1.5$ mm and 4 mm, i.e. $y/\delta = 0.06$ and 0.15 at $x/l = -0.04$, and $y/\delta = 0.08$ and 0.22 at $x/l = 0.86$, respectively, where δ is the boundary layer thickness. In terms of inner variables, corresponding values are $y^+ = 73$ and 193 and $y^+ = 125$ and 335, where $y^+ = y/\delta_\nu$ and $\delta_\nu = \nu/u_\tau$. The lower y is the nearest wall-parallel plane that could be conveniently accessed using a ∼1 mm thick laser sheet. A 527 nm Nd:YLF laser sheet and 13 μm silver-coated hollow glass spheres ($\rho_p = 1600$ kg m^{-3}, $St < 0.06$) are used for these measurements. Images are recorded by a pco.dimax CMOS high-speed camera, which has a pixel pitch of 11 μm and a maximum sensor size of 2016 × 2016 pixels^2. To achieve adequate spatial and temporal resolutions, data are recorded at 5000 fps using sensor configurations of 1296 × 720 pixels^2 and 816 × 1012 pixels^2 for the x–y and x–z planes, respectively. During analysis, these images are enhanced using modified histogram equalization, and the velocity fields are calculated using the LaVision DaVis® software. The final Δ is 32 × 32 pixels^2 (740 × 740 μm^2), with 75 % overlap between windows. To study the effect of resolution, we also calculate the velocity fields using the in-house program, as it allows use of rectangular correlation windows. Results for 32 × 32 and 32 × 16 pixels^2 windows are then compared, where the shorter dimension is aligned with the wall-normal direction. More than 13 000 velocity fields, obtained over a period of 2.74 s, are used to obtain flow statistics. For these measurements, the field of view does not cover the entire boundary layer. Consequently, we have also recorded lower resolution, time-resolved data at 3500 fps, and analysed it using

Location	$x_1/l=-0.04$	$x_2/l=0.14$	$x_3/l=0.29$	$x_4/l=0.4$	$x_5/l=0.52$	$x_6/l=0.63$	$x_7/l=0.75$	$x_8/l=0.88$
Δ (μm)	383	383	344	344	300	300	249	249
Vector spacing (μm)	191.5	191.5	172	172	150	150	124.5	124.5
Δ/δ_ν	38.6	37.6	33.8	36.3	35.7	41.2	38.0	43.7
$U_0(x)$ (m s^{-1})	2.97	3.1	3.31	3.52	3.75	4.06	4.4	4.88
$\delta(x)$ (mm)	22.55	22.73	23.84	22.3	20.04	19.41	18.15	17.49
$\theta(x)$ (mm)	1.96	1.76	1.51	1.26	1.07	0.88	0.77	0.65
$Re_\theta(x)$	5285	4946	4547	4026	3643	3241	3079	2900
$K(x)\times 10^6$	0.02	0.43	0.51	0.57	0.54	0.62	0.57	0.65
$u_\tau(x)$ (m s^{-1})	0.111	0.108	0.108	0.116	0.131	0.151	0.168	0.193
$u_\tau(x)/U_0(x)$	0.037	0.035	0.033	0.033	0.035	0.037	0.038	0.040
δ^+	2276	2232	2341	2352	2387	2664	2772	3069
$\kappa(x)$, assumed	0.41	0.42	0.422	0.422	0.422	0.422	0.422	0.422
ΔU^+_{max}	2.02	1.8	1.14	0.35	−0.9	−1.71	−2.16	−2.62
$\int_0^1 (\partial U/\partial x)\delta/U_0 \mathrm{d}(y/\delta)$	0.006	0.033	0.042	0.044	0.042	0.045	0.045	0.045

TABLE 1. Measurement resolutions and boundary layer global parameters at different streamwise locations for $Re_\theta(x_1)=5285$.

Location	$x/l = -0.04$	$x/l = 0.86$
$\varDelta$ (μm), high-resolution	740	740
Vector spacing (μm), high-resolution	185	185
$\varDelta/\delta_\nu$, high-resolution	35.8	61.9
$\varDelta$ (μm), low-resolution	1068	1068
Vector spacing (μm), low-resolution	267	267
$\varDelta/\delta_\nu$, low-resolution	51.7	89.3
$U_0(x)$ (m s^{-1})	1.37	2.16
$\delta(x)$ (mm)	26.76	17.8
$\theta(x)$ (mm)	2.698	0.814
$Re_\theta(x)$	3360	1598
$K(x)$	0.05×10^{-6}	1.28×10^{-6}
$u_\tau(x)$ (m s^{-1})	0.053	0.092
$u_\tau(x)/U_0(x)$	0.039	0.043
δ^+	1294	1489
$\kappa(x)$	0.41 (assumed)	0.68
ΔU^+_{max}	2.55	−0.21
$\int_0^1 (\partial U/\partial x)\delta/U_0 \mathrm{d}(y/\delta)$	0.006	0.04
$(\partial U/\partial y)\delta/U_0\vert_{wall}$	50.3	63.4

TABLE 2. Measurement resolutions and boundary layer global parameters for the time-resolved PIV measurements in ZPG and FPG boundary layers for $Re_\theta(x_1) = 3360$.

$\varDelta = 32 \times 32$ pixels^2 (1068×1068 μm^2) and 75 % overlap between windows. The results are used for calculating the global flow parameters, such as $U_0(x)$, $K(x)$, $\delta(x)$, $\theta(x)$ and $Re_\theta(x)$, as summarized in table 2. After calculating the local velocity distributions, to present profiles of mean velocity and turbulence parameters, we average the data over 21 streamwise grid points centred at the specified x/l.

In-line digital holographic microscopy (DHM) is performed to measure the wall shear stress in the $Re_\theta(x_1) = 3360$ FPG boundary layer, at a magnification that resolves the viscous sublayer. Details of the optical set-up, image processing and particle tracking methods can be found in Sheng, Malkiel & Katz (2008) and Sheng *et al.* (2009), and the methodology involved with implementation in the present facility is discussed in Talapatra & Katz (2012, 2013). A schematic of the optical set-up is shown in figure 2. A spatially filtered and collimated Nd:YAG laser beam illuminates the flow. Light scattered by the tracer particles interferes with the undisturbed part of the original beam to produce a hologram. The holograms are magnified by 10×, and recorded on the 4864×3248 pixels^2 CCD camera at a resolution of 0.73 μm pixel^{-1}. The flow is seeded with 1–6 μm diameter silver-coated glass spheres, which are injected at a velocity of 0.05 U_0 from sixteen 200 μm diameter holes, located 40 mm, i.e. 200 hole diameters, upstream of the sample volume. Holograms are numerically reconstructed in wall-normal steps of 4 μm, followed by 3D segmentation to obtain the particle coordinates. Particle tracking is used to obtain 3D velocity vectors on an unstructured grid. Data are analysed only in the viscous sublayer and part of the buffer layer ($y < 350$ μm, $y^+ < 29$). The mean velocity profile obtained from 107 statistically independent realizations, each containing 800–2200 matched particle pairs, is used to calculate the mean wall shear stress, τ_w.

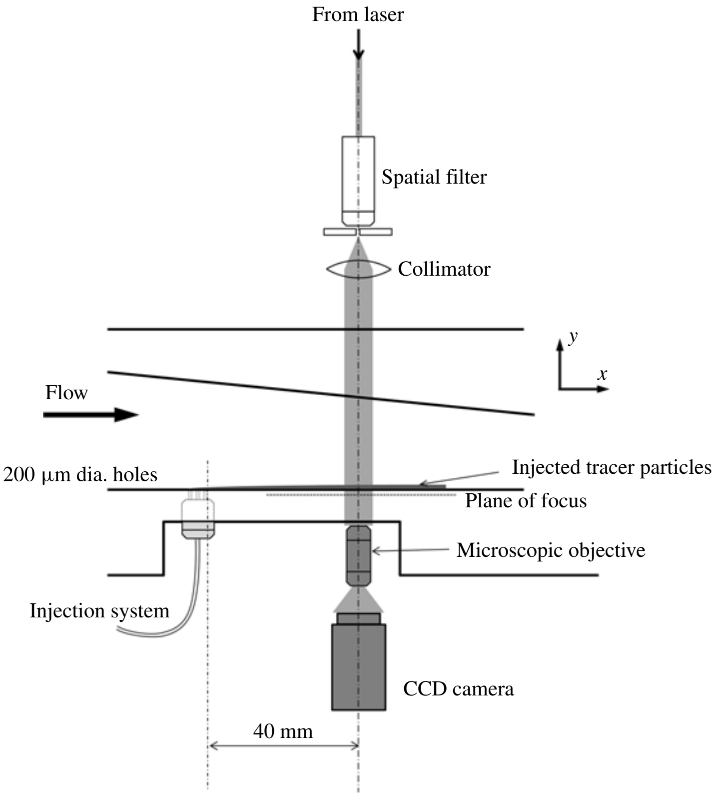

FIGURE 2. Optical set-up for DHM.

2.2. *Calculation of pressure fields*

Instantaneous pressure distributions are calculated by integrating the in-plane projection of the fluid material acceleration,

$$\frac{\mathrm{D}u}{\mathrm{D}t} = -\frac{1}{\rho}\frac{\partial p}{\partial x} + \nu\nabla^2 u; \quad \frac{\mathrm{D}v}{\mathrm{D}t} = -\frac{1}{\rho}\frac{\partial p}{\partial y} + \nu\nabla^2 v. \tag{2.1a,b}$$

We neglect the viscous terms, as the ratios of their standard deviations to the corresponding material acceleration terms are less than 0.02, based on 1000 realizations and averaging over the entire domain. Acceleration at time t_n is calculated using images I_{n-2}, I_{n-1}, I_n, I_{n+1}, I_{n+2} recorded at t_{n-2}, t_{n-1}, t_n, t_{n+1}, t_{n+2}, respectively, with constant time interval, δt, between them. The instantaneous particle displacement $(\boldsymbol{d}_{n,n+1})(\boldsymbol{x}_0)$ is obtained by correlating I_n with I_{n+1}, where $\boldsymbol{x}_0$ is the centre of an interrogation window in I_n. Similarly, $(\boldsymbol{d}_{n,n-1})(\boldsymbol{x}_0)$ is calculated using I_n and I_{n-1}. The velocity of the group of particles located at $\boldsymbol{x}_0$ at instant t_n is estimated as

$$\boldsymbol{u}_n = (\boldsymbol{d}_{n,n+1} - \boldsymbol{d}_{n,n-1})/(2\delta t). \tag{2.2}$$

Since the particles are displaced between exposures, the material acceleration is estimated from

$$\frac{\mathrm{D}\boldsymbol{u}_n}{\mathrm{D}t}(\boldsymbol{x}_0, t_n) \approx \frac{\boldsymbol{u}_{n+1}(\boldsymbol{x}_0 + \boldsymbol{d}_{n,n+1}, t_{n+1}) - \boldsymbol{u}_{n-1}(\boldsymbol{x}_0 + \boldsymbol{d}_{n,n-1}, t_{n-1})}{2\delta t}. \tag{2.3}$$

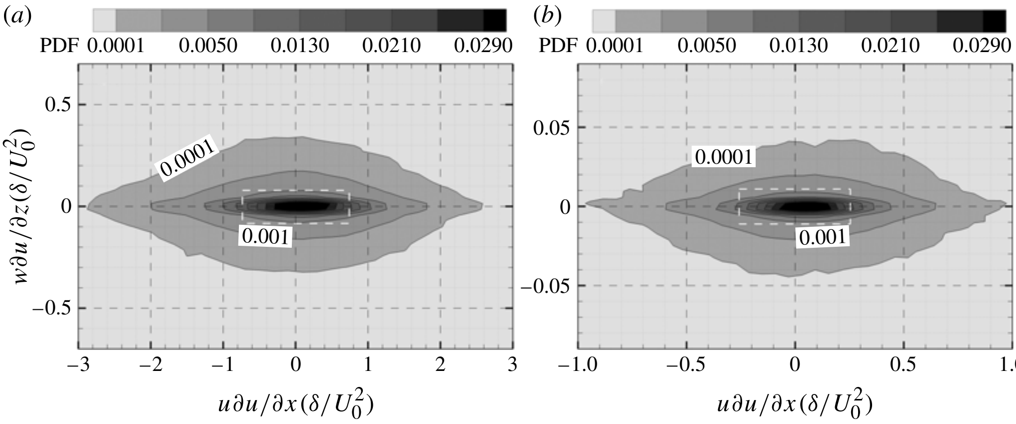

FIGURE 3. PDF of streamwise and spanwise convective acceleration terms at (*a*) $y/\delta = 0.15$ in the ZPG boundary layer and (*b*) $y/\delta = 0.22$ in the FPG boundary layer. White dashed rectangles indicate r.m.s. values.

Since we record planar data, our analysis does not account for the 3D displacement of the particles. The x–z plane measurements at, for example, $y = 4$ mm allow us to assess the magnitude of the spanwise (out-of-plane for x–y plane data) contribution to the material acceleration by comparing the magnitudes of $w\partial u/\partial z$ to those of $u\partial u/\partial x$, as shown in figure 3. The dimensions of the white dashed rectangle correspond to twice the standard deviations of the respective acceleration terms. It is clear that the spanwise term is significantly smaller than the streamwise term – for example, by 9.1 and 23.3 times for the ZPG and FPG boundary layers, respectively. The corresponding values at $y = 1.5$ mm are 6.98 and 18.2, indicating that the spanwise contribution increases close to the wall.

To obtain pressure, we use an omni-directional virtual boundary integration scheme (Liu & Katz 2006, 2013). Since pressure is a scalar, spatial integration of the pressure gradient must be independent of the integration path. The integration starts from and stops at the real boundaries, along paths originating from and ending at discrete points distributed uniformly, every 0.3°, along a circular virtual boundary that surrounds the PIV area. Averaging the results of all the integration paths for each internal node minimizes the uncertainty caused by local errors in the measured material acceleration. The pressure on the real boundary is initially obtained by line-integration along the real boundary, and is subsequently updated by the omni-integration results. Iterations lead to a converged boundary pressure distribution. Since the integration provides pressure along with an undetermined time-dependent constant, we can obtain $(p - p_{ref})(x, y, t)$ by arbitrarily selecting any point in the sample domain and using its pressure as p_{ref}. We opt to use the spatially averaged p over the entire calculation domain as p_{ref}. Accordingly, all the results presented in this paper involve $(p - p_{ref})$. To estimate the uncertainty in pressure due to the omission of the spanwise terms, we add to the planar material acceleration a randomly distributed Gaussian noise with a uniform standard deviation over the calculation domain (although out-of-plane effects are not random). Denoting the difference between $p - p_{ref}$ calculated with and without the noise by δp, the uncertainty in pressure is $e = \langle(\delta p)^2\rangle^{1/2}/\langle(p - p_{ref})'^2\rangle^{1/2}$. Assuming a standard deviation of noise equal to that of $w\partial u/\partial z$ at $y = 4$ mm, results in $e = 8.6\,\%$ for the ZPG and $3.7\,\%$ for the FPG boundary layers, based on

1000 realizations and averaging over the entire domain. When the noise r.m.s. is increased to that of $w\partial u/\partial z$ at $y = 1.5$ mm, the corresponding values of e increase to 11.5 % and 6.8 %. These estimates agree with the impact of out-of-plane terms measured by Ghaemi *et al.* (2012). They report a correlation of 0.6 between the wall pressure measured by a transducer and that calculated from 3D acceleration, while the corresponding correlation for planar calculations is 0.48.

3. Results: Mean flow and turbulence statistics

3.1. *Mean velocity and Reynolds stresses*

At $x/l = -0.04$, there is a narrow 'freestream' region, which is approximately 7 mm and 12 mm wide for $Re_\theta(x_1) = 3360$ and 5285, respectively, between the top and bottom wall boundary layers. However, following Tsuji *et al.* (2012), due to the proximity between the top and bottom boundary layers, the pressure fluctuations in one might affect those in the other. Such effects are more consistent with channel flows. Due to the asymmetry in boundary conditions, $\partial U/\partial y$ in the freestream is not zero, but is very small, less than 0.3 % of $\partial U/\partial y_{max}$. Hence, the boundary layer edge, where U_0 is determined, is defined as the point where $\partial U/\partial y$ drops below a threshold of 0.015 $U_0(x_1)/h$ for $Re_\theta(x_1) = 5285$ and 0.04 $U_0(x_1)/h$ for $Re_\theta(x_1) = 3360$, where h is the half channel height at x_1. The different thresholds reflect variations in minima attained by $\partial U/\partial y$. Figure 4 shows the streamwise evolution of the acceleration parameter and the Reynolds number. To calculate K, $\mathrm{d}U_0/\mathrm{d}x$ is obtained by linear least-square fits to $U_0(x)$ over 0.55-0.7δ long domains centred at each x/l. For both Reynolds numbers, K is very small at $x/l = -0.04$, allowing us to use it as the reference ZPG site. For $Re_\theta(x_1) = 5285$, the acceleration parameter rises to a plateau of $\sim 0.6 \times 10^{-6}$ at $x/l > 0.3$, while for $Re_\theta(x_1) = 3360$, $K_{x/l=0.86} = 1.3 \times 10^{-6}$. Both values are only 9 % higher than those based on potential flow calculations and, by construction, are well below the relaminarization level. For both Reynolds numbers, Re_θ decreases with increasing x/l, but it does not reach the corresponding equilibrium values of 1600 and 840, predicted by Jones, Marusic & Perry (2001). In spite of the plateau in K, the sink flow is not long enough for the boundary layers to reach equilibrium.

To estimate the friction velocity from the log region data at $x/l = -0.04$, we assume $\kappa = 0.41$. In the FPG region, for $Re_\theta(x_1) = 3360$, we calculate u_τ using two methods: by direct measurement of $\partial U/\partial y$ at the wall from the DHM data, and by performing a 2D momentum analysis,

$$\begin{aligned} \tau_w l_{CV} &= \left\{ \int_0^{0.88\delta} \left[(P - P_{ref}) + \rho U^2 + \rho \langle u'^2 \rangle \right] \mathrm{d}y \right\}_{x=x_U} \\ &\quad - \left\{ \int_0^{0.88\delta} \left[(P - P_{ref}) + \rho U^2 + \rho \langle u'^2 \rangle \right] \mathrm{d}y \right\}_{x=x_D} \\ &\quad - \left\{ \int_{x_U}^{x_D} \left[\rho UV + \rho \langle u'v' \rangle \right] \mathrm{d}x \right\}_{y=0.88\delta}. \end{aligned} \tag{3.1}$$

Here x_U, x_D are the upstream and downstream boundaries, respectively, of a control volume of length $l_{CV} = 0.88\delta$. This balance accounts for the variation of $\partial P/\partial x$ across the boundary layer, which, as shown later, is ± 12 %. Figure 5 shows the probability distribution function (PDF) of u obtained from DHM data over a volume of 3.51 mm $\times$ 0.34 mm $\times$ 2.34 mm ($293\delta_\nu \times 28\delta_\nu \times 195\delta_\nu$) in the x, y and

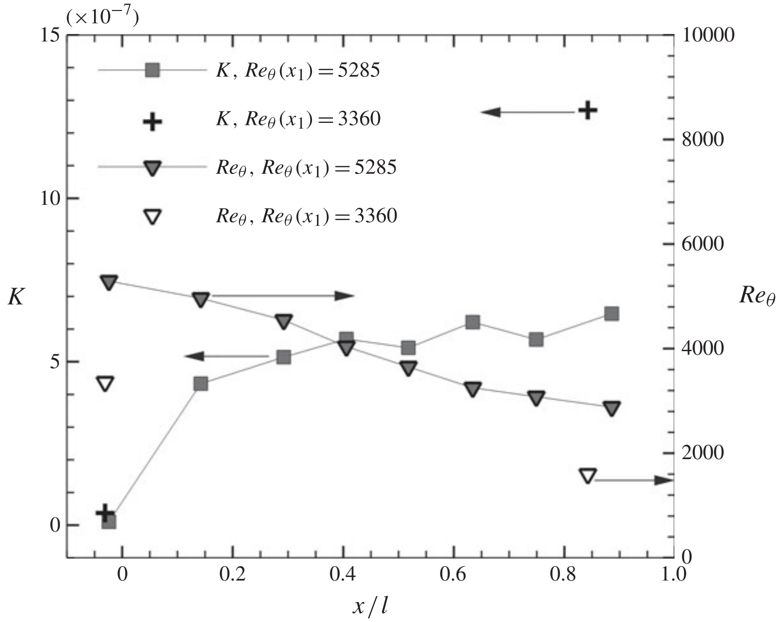

FIGURE 4. Streamwise development of K and Re_θ.

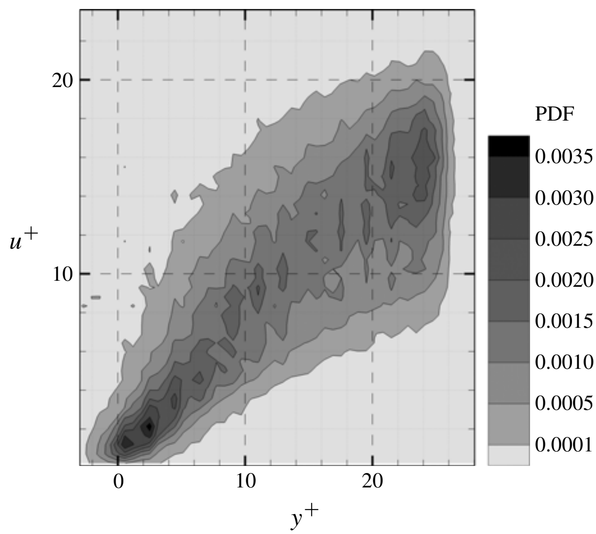

FIGURE 5. PDF of near-wall instantaneous streamwise velocity measured by DHM at $x/l = 0.86$ and $Re_\theta(x_1) = 3360$.

z directions, respectively. The mean velocity gradient at the wall is calculated by fitting a second-order polynomial to the data at $y^+ < 3$, since close to the wall, $\nu\partial^2 U/\partial y^2 \approx (1/\rho)\partial P/\partial x$. The result, $u_\tau/U_0 = 0.043$, agrees with the one obtained from momentum balance within 0.5 %. Using u_τ, we calculate the corresponding value of κ by a line fit through the log region. Results are included in table 2. Although κ is higher than that expected for equilibrium conditions (Dixit & Ramesh 2008), it falls within the previously obtained range (Bourassa & Thomas 2009) for similar values of K without equilibrium. Since we do not have DHM data for $Re_\theta(x_1) = 5285$, we estimate u_τ/U_0 by assuming equilibrium values of κ for the corresponding acceleration parameters, following Dixit & Ramesh (2008). As is evident from the result for $Re_\theta(x_1) = 3360$, this assumption might lead to underestimation of u_τ for non-equilibrium FPG boundary layers. Consequently, these estimates are used only for presenting mean velocity profiles, and subsequent $Re_\theta(x_1) = 5285$ data are normalized only by δ and U_0.

A comparison between velocity profiles is presented in figure 6(*a*).In the log region, the ZPG profiles fall slightly above the universal law $U^+ = (1/0.41)\ln y^+ + B$ ($B = 5.3$, Pope 2000), giving $B = 6.1$. For the $Re_\theta(x_1) = 3360$ FPG boundary layer, the plot includes both DHM and PIV results. As expected, in the viscous sublayer the profile lies below the $U^+ = y^+$ curve, since $\partial U/\partial y$ decreases with increasing elevation. For both Reynolds numbers, the FPG profiles have log regions, and dip below the log fits away from the wall, in agreement with previous studies for non-equilibrium boundary layers (e.g. Patel & Head 1968; Badri Narayanan & Ramjee 1969; Escudier *et al.* 1998). Streamwise variations in velocity profiles for $Re_\theta(x_1) = 5285$ are shown in figure 6(*b*). As the flow accelerates, the profiles initially shift upward, peaking at $x/l \sim 0.4$, and then reverse trend further downstream. However, the log regions remain above that of the ZPG boundary layer. These trends may occur in part as a result of the assumed values of κ, but are consistent with trends of Reynolds shear stresses, discussed later. Values of the wake parameter, defined as $\Delta U^+_{max} = \max\{U^+ - [(1/\kappa)\ \ln y^+ + B]\}$, are provided in tables 1 and 2. In using the term 'max', we refer to the magnitude, but keep the sign of the term in the bracket. In the ZPG area, for both Reynolds numbers, the distribution of the wake function agrees with the classical relation $\Delta U^+ = \Delta U^+_{max} \sin^2(\pi y/2\delta)$ (Gad-el-hak & Bandyopadhyay 1994; Pope 2000), and ΔU^+_{max} falls within the expected range (Fernholz & Finley 1996). The profiles increasingly deviate from this relation with increasing x/l, where ΔU^+_{max} decreases monotonically, becoming negative for $x/l > 0.4$. For a later discussion of mean velocity gradient effects on alignment of turbulent structures, figure 7 shows $\partial U/\partial y(\delta/U_0)$ for $Re_\theta(x_1) = 3360$, assuming $U^+ = y^+$ at the wall in the ZPG boundary layer. Results for the higher Reynolds number display similar trends (not shown). As is evident, when normalized by $U_0(x)/\delta(x)$, the near-wall shear in the FPG region is only slightly higher than that in the ZPG boundary layer (table 2). The ratio of the actual magnitudes at the wall is 2.99. The values of $\partial U/\partial x(\delta/U_0)$, which represents streamwise stretching, are largely constant across the boundary layers (not shown), and are significantly higher in the FPG domain (~0.04) than those in the ZPG boundary layer (~0.006).

Figure 8 compares profiles of Reynolds stresses. Trends in the ZPG domain are similar to those observed in previous studies (e.g. Spalart 1988; Fernholz & Finley 1996). However, the profiles do not collapse when normalized either with U_0 (except for the outer layer $\langle u'u'\rangle$) or with u_τ (results not shown). These trends might be affected by the limited spatial resolution of measurements. As an example, figure 9 compares $\langle u'v'\rangle$ obtained using the regular $740 \times 740\ \mu m^2$ windows to that obtained using $740 \times 370\ \mu m^2$ windows. Results are indistinguishable in the outer layer. However, doubling the wall-normal resolution increases $\langle u'v'\rangle$ by 6 % at $y/\delta \sim 0.04$ in the ZPG boundary layer. The change is significantly higher (20 %) near the wall of the FPG region, presumably since the normalized resolution there is lower. The limited resolution affects the near-wall trends, but not those in the outer layer, consistent with prior studies (e.g. Ligrani & Moffat 1986; Shah, Agelinchaab & Tachie 2008).

Figures 8 and 9 indicate that all the locally normalized stresses in the FPG boundary layer are much weaker than those in ZPG conditions, in agreement with previous

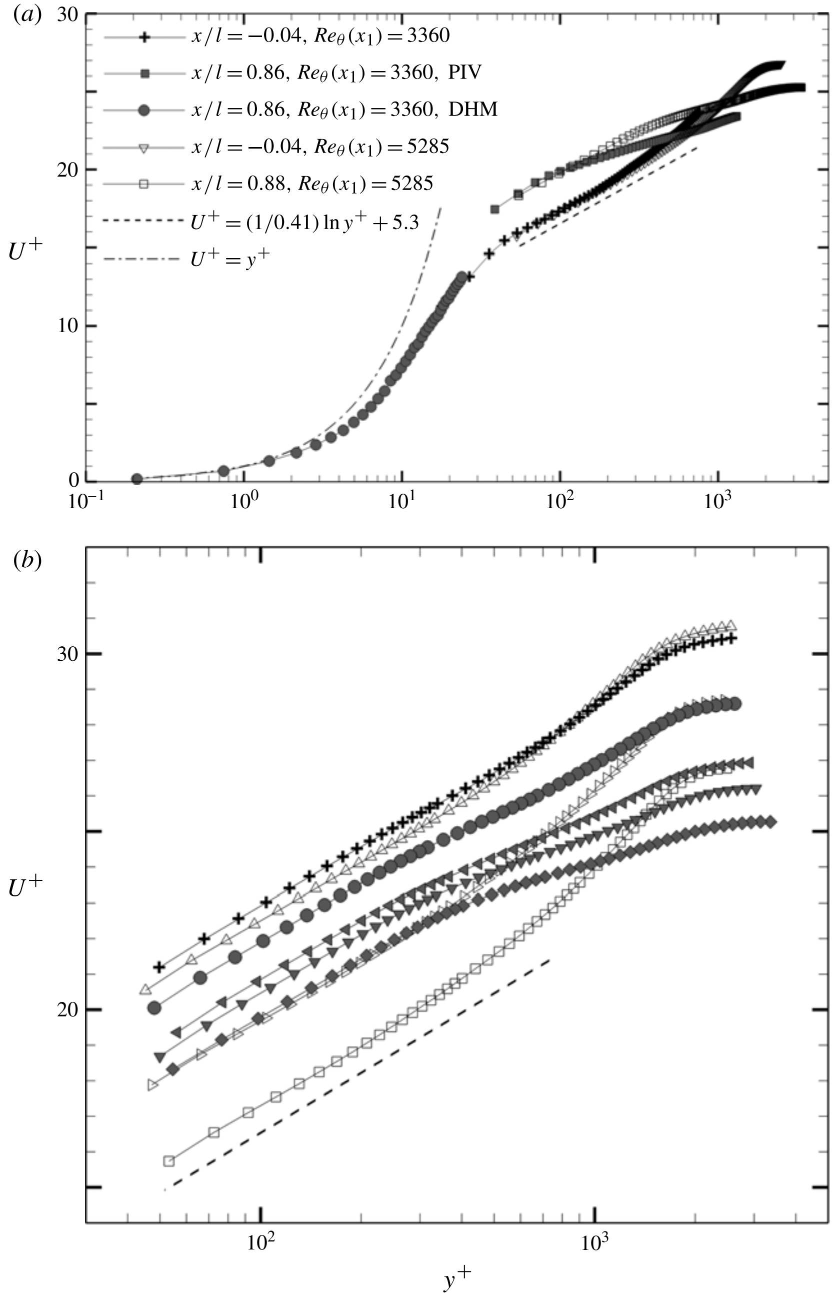

FIGURE 6. Mean velocity profiles (*a*) in the ZPG and FPG boundary layers and (*b*) at different streamwise locations for $Re_\theta(x_1) = 5285$. In (*b*), —□—, $x/l = -0.04$; —▷—, $x/l = 0.14$; —△—, $x/l = 0.29$; —+—, $x/l = 0.4$; —●—, $x/l = 0.52$; —◀—, $x/l = 0.63$; —▼—, $x/l = 0.75$; —◆—, $x/l = 0.88$; ------, $U^+ = (1/0.41)\ln y^+ + 5.3$. In (*b*), only a fraction of the data points are shown to make trends discernible.

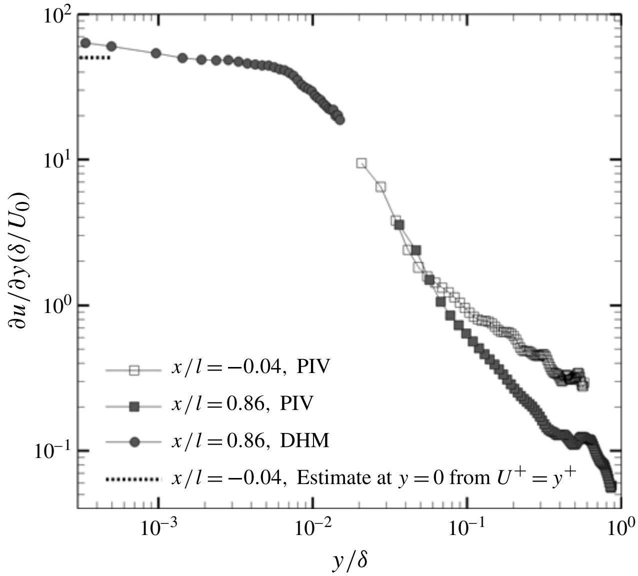

FIGURE 7. Profiles of $\partial U/\partial y(\delta/U_0)$ for $Re_\theta(x_1) = 3360$.

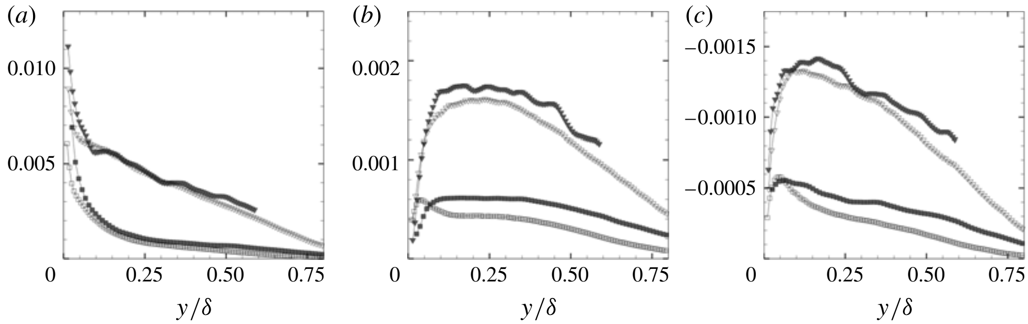

FIGURE 8. Reynolds stresses: (*a*) $\langle u'u'\rangle/U_0^2(x)$, (*b*) $\langle v'v'\rangle/U_0^2(x)$ and (*c*) $\langle u'v'\rangle/U_0^2(x)$. ▼, $x/l = -0.04$, $Re_\theta(x_1) = 3360$; ■, $x/l = 0.86$, $Re_\theta(x_1) = 3360$; ▽, $x/l = -0.04$, $Re_\theta(x_1) = 5285$; □, $x/l = 0.88$, $Re_\theta(x_1) = 5285$.

studies (e.g. Jones & Launder 1972; Ichimiya *et al.* 1998). The streamwise evolution of $\langle u'v'\rangle/U_0^2$ for $Re_\theta(x_1) = 5285$ (figure 10*a*) shows that the shear stress decays over most of the boundary layer as the flow accelerates, but appears to collapse close to the wall ($y/\delta < 0.06$) in the region of constant K. Corresponding profiles of $\langle u'u'\rangle$ and $\langle v'v'\rangle$ (not shown) exhibit similar trends. To demonstrate the evolution of actual stress magnitude, the same data is normalized by $U_0(x_1)$ in figure 10(*b*). Initially, at $-0.04 \leqslant x/l \leqslant 0.40$, the stress decays over the entire boundary layer, and the peak is broad. Further downstream, in the region of constant K, the stress continues to decay in the outer part, but increases substantially close to the wall ($y/\delta \leqslant 0.15$). Thus, although the limited resolution is expected to have greater effect on the near-wall stress in the FPG region, $\langle u'v'\rangle$ close to the wall is still higher than that in the ZPG boundary layer. The trends for $\langle u'u'\rangle$ and $\langle v'v'\rangle$, as well as for the lower Reynolds number case (not shown), are similar. The increase in stresses in a narrow near-wall region, which indicates generation of new turbulence that does not diffuse outward, has been

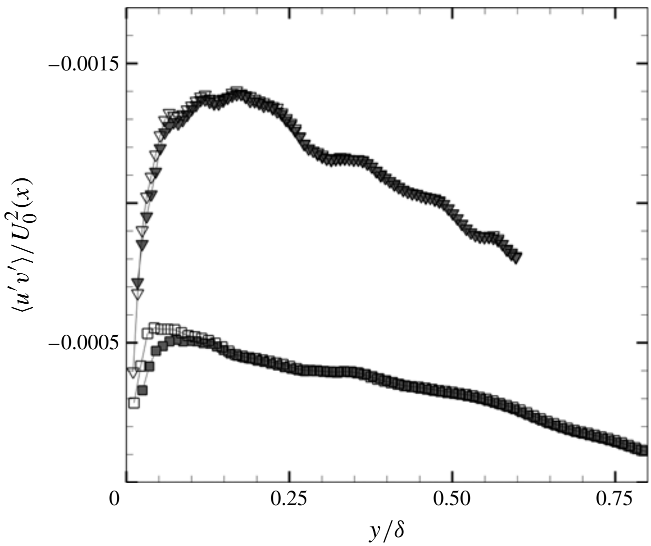

FIGURE 9. Effect of interrogation window size on profiles of Reynolds shear stress; $Re_\theta(x_1) = 3360$. —▼—, ZPG, $\Delta = 32 \times 32$ pixels^2; —▽—, ZPG, $\Delta = 32 \times 16$ pixels^2; —■—, FPG, $\Delta = 32 \times 32$ pixels^2; —□—, FPG, $\Delta = 32 \times 16$ pixels^2.

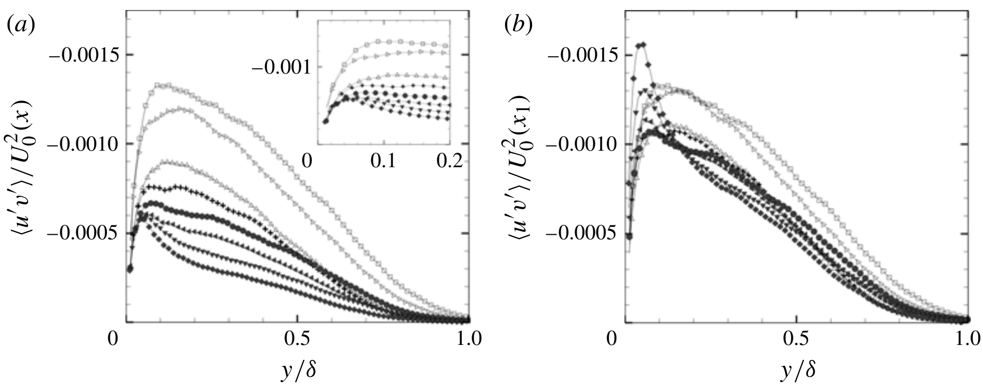

FIGURE 10. Reynolds shear stresses for $Re_\theta(x_1) = 5285$ normalized by: (*a*) local freestream velocity and (*b*) freestream velocity at the inlet to the sink flow region. —□—, $x/l = -0.04$; —▷—, $x/l = 0.14$; —△—, $x/l = 0.29$; —+—, $x/l = 0.4$; —●—, $x/l = 0.52$; —◀—, $x/l = 0.63$; —▼—, $x/l = 0.75$; —◆—, $x/l = 0.88$. Only alternate data points are shown. Inset in (*a*) shows a magnified view of the near-wall region.

observed in several previous studies (e.g. Escudier *et al.* 1998; Bourassa & Thomas 2009). Finally, for both Reynolds numbers, u_τ^2 is higher than the peak $|\langle u'v'\rangle|$ by less than 5 % at $x/l = -0.04$ (tables 1 and 2). Further downstream, $|\langle u'v'\rangle|_{max}/u_\tau^2$ decays to below 0.4 in the FPG boundary layers, consistent, for example, with Bourassa & Thomas (2009).

3.2. *Statistics for pressure and pressure gradient*

Figure 11 presents profiles of mean pressure and pressure gradient, and compares data obtained by integrating the instantaneous material acceleration, P, to that obtained by

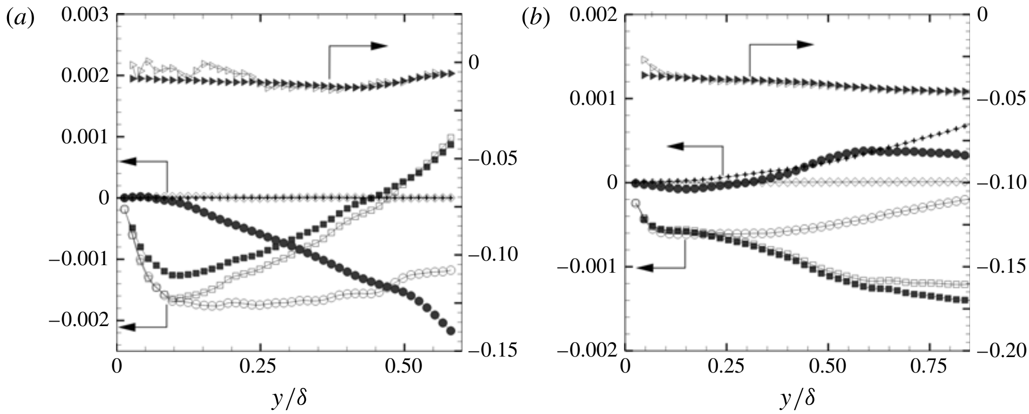

FIGURE 11. Mean pressure (left ordinate) and mean pressure gradient (right ordinate) in the (*a*) ZPG and (*b*) FPG boundary layers for $Re_\theta(x_1) = 3360$. open triangle, $(\partial \boldsymbol{P}/\partial x)(\delta/\rho U_0^2)$; filled triangle, $(\partial P/\partial x)(\delta/\rho U_0^2)$; open square, $(\boldsymbol{P} - P_{wall})/(\rho U_0^2)$; filled square, $(P - P_{wall})/(\rho U_0^2)$; open circle, $-\langle v'v'\rangle/U_0^2$; filled circle, $\int_0^y [(1/U_0^2)U\partial V/\partial x]\mathrm{d}y$; plus, $\int_0^y [(1/U_0^2)V\partial V/\partial y]\mathrm{d}y$; open diamond, $\int_0^y [(1/U_0^2)\partial\langle u'v'\rangle/\partial x]\mathrm{d}y$. Only alternate data points are shown.

integrating the Reynolds-averaged Navier–Stokes equation,

$$\boldsymbol{P}(y) = P_{wall} - \rho\langle v'v'\rangle(y) - \rho\int_0^y \left[U\frac{\partial V}{\partial x} + V\frac{\partial V}{\partial y} + \frac{\partial\langle u'v'\rangle}{\partial x}\right]\mathrm{d}y, \tag{3.2}$$

where viscous terms are neglected, and P_{wall} is averaged over the lowest interrogation window ($10 \leqslant y^+ \leqslant 45$ and $15 \leqslant y^+ \leqslant 77$ for the ZPG and FPG flows, respectively). In both cases, $\boldsymbol{P} - P_{wall}$ and $P - P_{wall}$, as well as $\partial\boldsymbol{P}/\partial x$ and $\partial P/\partial x$, follow each other closely, but the omni-directional results are smoother, presumably since they are less sensitive to uncertainties in the small v close to the wall (0.01 pixel in the ZPG, and < 0.1 pixel in the FPG boundary layer). According to the 2D boundary layer approximation, $P - P_{wall} \sim -\rho\langle v'v'\rangle$. However, in the present results, $P - P_{wall}$ follows $-\rho\langle v'v'\rangle$ closely only near the wall. In the outer layer, $U\partial V/\partial x$ becomes significant in the ZPG flow, and both convective terms contribute in the FPG boundary layer. The contribution of the shear stress is negligible in both cases. Yet, in the FPG domain, $\partial P/\partial y$ (not shown) is still an order of magnitude smaller than $\partial P/\partial x$, except close to the wall ($y/\delta < 0.08$), where it increases to $\sim$22 % of $\partial P/\partial x$.

Figure 12(*a*) shows that $\sigma_{\partial p/\partial x} = \langle(\partial p'/\partial x)^2\rangle^{1/2}$ normalized by $\rho U_0^2(x)/\delta(x)$ in the ZPG region is substantially higher than that in the FPG boundary layer, and that, in both cases, $\sigma_{\partial p/\partial x}$ increases rapidly with decreasing y. However, when normalized by $\rho\langle u'u'\rangle(x,y)/\delta(x)$, profiles of both boundary layers collapse onto each other (figure 12*b*), and the magnitudes increase with distance from the wall. They do not collapse if we replace δ with δ_ν as the normalizing length scale (not shown). Similar to the behaviour of Reynolds stresses, un-scaled $\sigma_{\partial p/\partial x}$ in the FPG boundary layer is higher close to the wall and lower away from the wall in comparison to that in the ZPG region (also not shown). The profiles of $\sigma_p = \langle(p' - p'_{ref})^2\rangle^{1/2}$, shown in figures 13(*a*)–(*c*), inherently account only for fluctuations at scales smaller than our field of view. The rapid near-wall increase in σ_p for both boundary layers agrees with trends reported by Spalart (1988) and Tsuji *et al.* (2007). Very near the wall, σ_p is

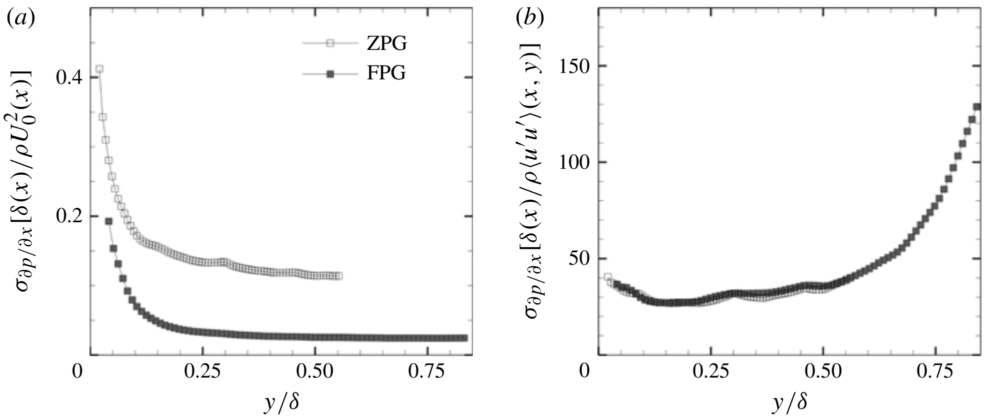

FIGURE 12. R.m.s. values of: (*a*) $(\partial p/\partial x)[\delta(x)/\rho U_0^2(x)]$ and (*b*) $(\partial p/\partial x)[\delta(x)/\rho\langle u'u'\rangle(x, y)]$.

expected to decrease (Spalart 1988; Jiménez & Hoyas 2008). Consequently, our σ_p at the lowest elevation for the ZPG case, which represents a spatial average over the lowest interrogation window, is higher than published wall pressure fluctuation results (e.g. Tsuji *et al.* 2007). However, in figure 13(*b*), the present values of $\sigma_p/\rho u_\tau^2$ are compared to those provided in previous studies for the log region. Our values are higher than the DNS results of Spalart (1988) for $Re_\theta = 1410$, but fall within the range measured by Tsuji *et al.* (2007) for $7420 < Re_\theta < 15\,200$. The ZPG pressure fluctuations are much higher than those of the FPG boundary layer, when scaled with $\rho U_0^2(x)$ or $\rho u_\tau^2(x)$ (figures 13*a*,*b*). Unlike the pressure gradients, the profiles do not collapse when scaled by $\rho\langle u'u'\rangle$ (figure 13*c*), but the difference between them is greatly reduced. At $0 \leqslant y/\delta \leqslant 0.5$, $\sigma_p/\rho\langle u'u'\rangle \sim 1$ for the ZPG case, in agreement with Tsuji *et al.* (2007). Spectra and PDFs of $p' - p'_{ref}$ at different elevations in the ZPG boundary layer are presented in figures 13(*d*) and 13(*e*), respectively. The spectra show a power law exponent of -1.6 in the outer layer. The wavenumber range for this behaviour $(0.016 < k_1\nu/u_\tau < 0.06)$ is smaller than, and roughly coincident with, that of Tsuji *et al.* (2007) at $Re_\theta \geqslant 5870$. Also in agreement with previous studies (e.g. Kim 1989; Tsuji *et al.* 2007), PDFs of $p' - p'_{ref}$ (figure 13*e*) exhibit higher peaks near zero, and larger tails than a Gaussian distribution. The skewness and flatness values are approximately -0.1 and 4, except at $y/\delta = 0.05$, where they are -0.07 and 5.6, respectively. The skewness values are lower in magnitude than the log region value of -0.3 reported by Tsuji *et al.* (2007). However, the flatness values are close to the value of 4.6 reported by them. The present FPG spectra and PDFs (not shown) exhibit similar trends.

4. Effect of mean FPG on instantaneous flow structures

Numerous studies have discussed the dynamics of packets of hairpin vortices in ZPG boundary layers, which appear as inclined trains of vortices in the x–y plane. These structures migrate away from the wall by self-induction, and play a dominant role in wall-normal momentum transport (Adrian, Meinhart & Tomkins 2000; Hutchins, Hambleton & Marusic 2005). Figure 14(*a*) shows an example of such a vortex train evident in the present ZPG boundary layer. Instantaneous data also confirms that hairpin packets often form in the FPG boundary layer, but remain

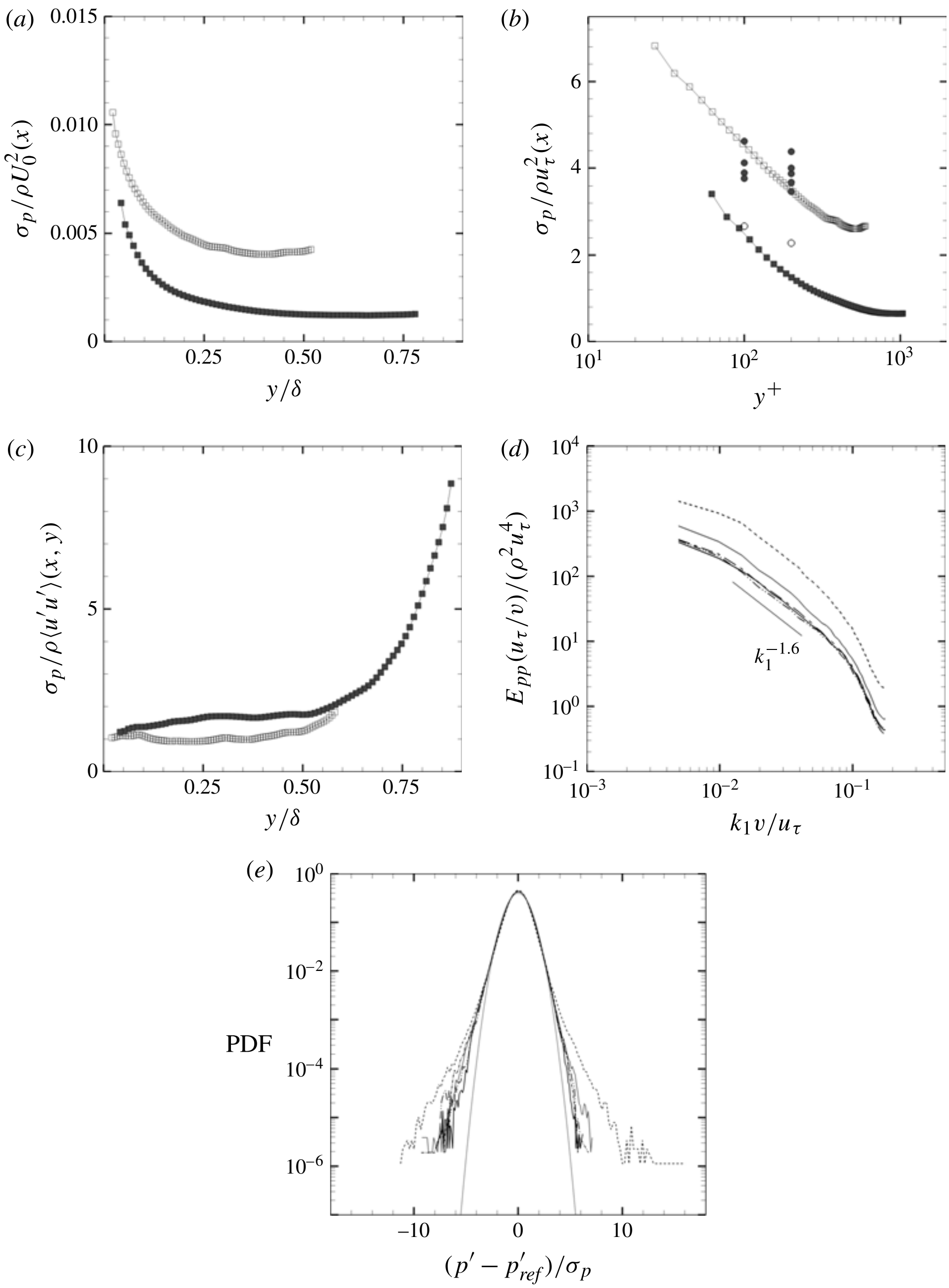

FIGURE 13. R.m.s. values of: (*a*) $(p-p_{ref})/\rho U_0^2(x)$, (*b*) $(p-p_{ref})/\rho u_\tau^2(x)$ and (*c*) $(p-p_{ref})/\rho\langle u'u'\rangle(x,y)$. —□—, ZPG boundary layer; —■—, FPG boundary layer; ○, Spalart (1988), $Re_\theta = 1410$; ●, Tsuji *et al.* (2007), $Re_\theta = 7420$–15 200. Spectra and PDFs for $p-p_{ref}$ at different elevations in the ZPG boundary layer are shown in (*d*) and (*e*), respectively. - - - - - -, $y/\delta = 0.05$; ———, $y/\delta = 0.18$; — · — · —, $y/\delta = 0.36$; ———, $y/\delta = 0.44$; — · · — · ·, $y/\delta = 0.53$. In (*e*), ··················, Gaussian distribution.

confined to the near-wall region and are inclined at shallow angles to the wall (figure 14*c*). Consequently, the outer layer frequently consists of extended regions of low turbulence. The shallow inclinations are in line with previous studies (e.g. Piomelli *et al.* 2000; Dixit & Ramesh 2010) and, as discussed later, are predominantly caused by the larger $\partial U/\partial y$ and $\partial U/\partial x$ relative to the vortex self-induction. As expected, the minima in the corresponding $p' - p'_{ref}$ distributions (figures 14*b*, 14*d*) coincide with the vortical structures, while the maxima show a preference for regions of elevated normal strain. Furthermore, $p' - p'_{ref}$ decays rapidly away from the wall in the FPG boundary layer, in agreement with figure 14(*c*).

A consistent picture is observed in the x–z planes. Figure 15(*a*) presents a sample of ω'_y and streamlines at $y/\delta = 0.06$ in the ZPG domain. Here, low-speed regions seem to be bounded by 'legs' of large-scale vortices, which appear as swirling streamline patterns, as reported in previous studies (e.g. Tomkins & Adrian 2003; Ganapathisubramani, Longmire & Marusic 2003). Figure 15(*b*) is a characteristic sample for the FPG case, at $y/\delta = 0.08$. It shows parallel, nearly continuous, streamwise-elongated regions with opposite sign ω_z, and low-speed streaks between them. This pattern suggests that the visualized plane dissects structures inclined at shallow angles. These elongated vortices are not observed at $y/\delta = 0.22$ (not shown), consistent with the x–y plane observations. In figure 15(*b*), it is much harder to identify the legs of large-scale structures, although broad regions of roughly circular streamlines cross the sample area frequently, e.g. at $14.55 < x/\delta < 15.25$. In the ZPG domain, small-scale structures are found everywhere, but more frequently inside low-speed regions. Conversely, in the FPG boundary layer, they are nearly absent in high-momentum regions, as sweeps ($u' > 0$, $v' < 0$) force outer layer fluid with low small-scale turbulence towards the wall. To calculate the width of the low-speed regions, Δz, u' is filtered by 1D moving box filters of width $T_B = 1.5\delta/U_0$ in time, and $W_B = 0.25\delta$ along x, to obtain large-scale fluctuations, $\widetilde{u'}$. The spatial filter size is limited by the overall extent of the measurement domain, while T_B is chosen to extract large-scale motions, which are discussed in § 6.1. Boundaries of low-speed regions are defined by $\widetilde{u'} = 0$ and require $\widetilde{u'} < -0.5\sigma_{\widetilde{u}}$ within them, where $\sigma_{\widetilde{u}}$ is the standard deviation of $\widetilde{u'}$. Our analysis indicates that this threshold, as well as the filter sizes, have little impact on the reported trends. The PDFs of Δz at $y = 1.5$ mm (figure 16) show that un-scaled Δz values for both boundary layers are similar. Since the ZPG site is located $10.5\delta(x_1)$ upstream of the FPG region, it is possible that some of the FPG low-speed regions are formed in the ZPG area. Mean values, modes and r.m.s. of Δz are summarized in table 3, including data for $y = 4$ mm. Here again, Δz is not significantly different between the two flows, suggesting causality, but it increases with increasing elevation, consistent with reported trends for ZPG flows (Tomkins & Adrian 2003; Hutchins & Marusic 2007).

5. Two-point correlations of velocity and pressure fluctuations

We analyse two-point correlations among variables φ and ψ,

$$R_{\varphi,\psi}(x_0, y_0, x, y) = \langle \varphi'(x_0, y_0) \cdot \psi'(x, y)\rangle / [\sigma_\varphi(x_0, y_0) \cdot \sigma_\psi(x, y)], \tag{5.1}$$

to further ascertain the impact of FPG on the flowstructure. Here, σ_φ and σ_ψ are the standard deviations of φ and ψ, respectively, and (x_0, y_0) is the reference location. The ZPG results for $R_{u,u}$ (figures 17*a*,*b*) show the inclined eddy structure observed before numerous times (e.g. Tutkun *et al.* 2009), and has been attributed to hairpin packets

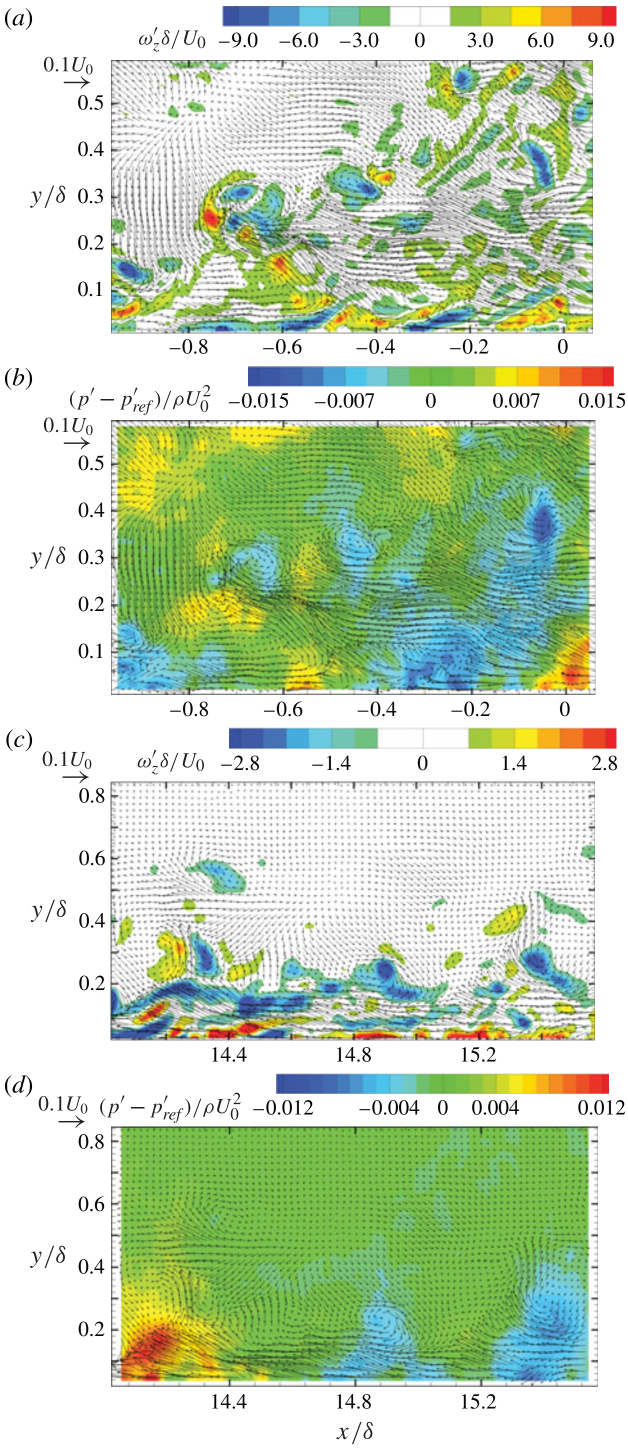

FIGURE 14. Sample instantaneous distributions of (*a* and *c*) $\omega_z'\delta/U_0$ and vectors of $(u'/U_0, v'/U_0)$; (*b* and *d*) $(p' - p'_{ref})/\rho U_0^2$. Distributions are taken in the (*a* and *b*) ZPG and (*c* and *d*) FPG boundary layers. Only alternate vectors are shown.

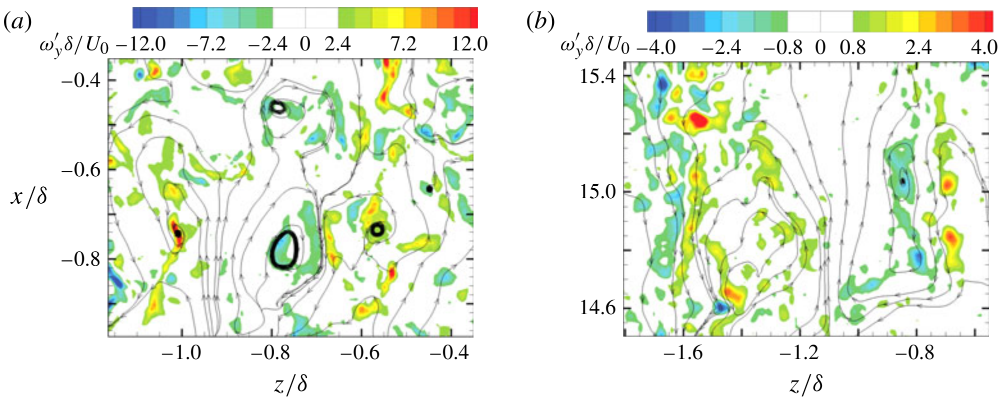

FIGURE 15. Sample snapshots of wall-normal vorticity and streamlines in x–z planes, for (*a*) ZPG boundary layer at $y/\delta = 0.06$ ($y^+ = 73$) and (*b*) FPG boundary layer at $y/\delta = 0.08$ ($y^+ = 125$).

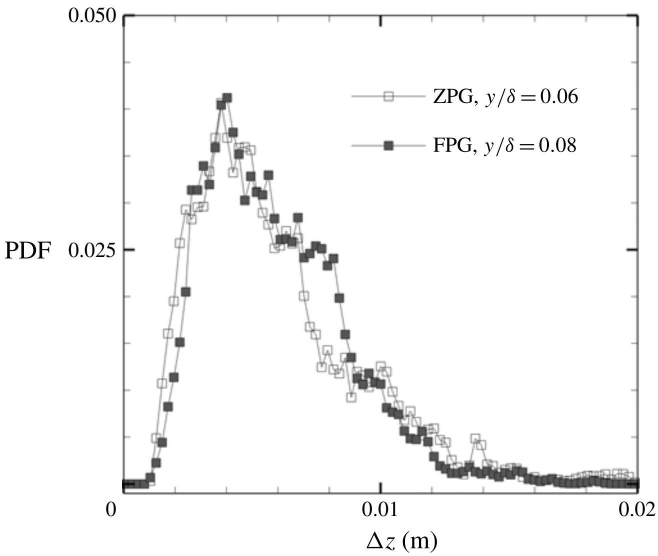

FIGURE 16. PDFs of the width of low-speed regions at $y = 1.5$ mm.

(Guala, Metzger & McKeon 2011). A similar structure in figure 17(*c*) suggests that these packets also contribute significantly to $R_{u,u}$ near the wall of the FPG region. However, the inclination angle is shallower than that for the ZPG case, consistent with the orientation of near-wall vortex trains, the reasons for which are discussed below. The angle increases with y_0 in the ZPG domain, but decreases with increasing elevation in the FPG boundary layer. This trend is likely a result of the near-wall confinement of the hairpin packets (figure 14*c*), which essentially eliminates the primary mechanism of wall-normal momentum transport, in agreement with low outer layer $\langle u'v'\rangle$. Furthermore, as the outer region is left with only large-scale turbulence, the correlation lengths increase more rapidly with increasing y_0 in comparison to the ZPG case.

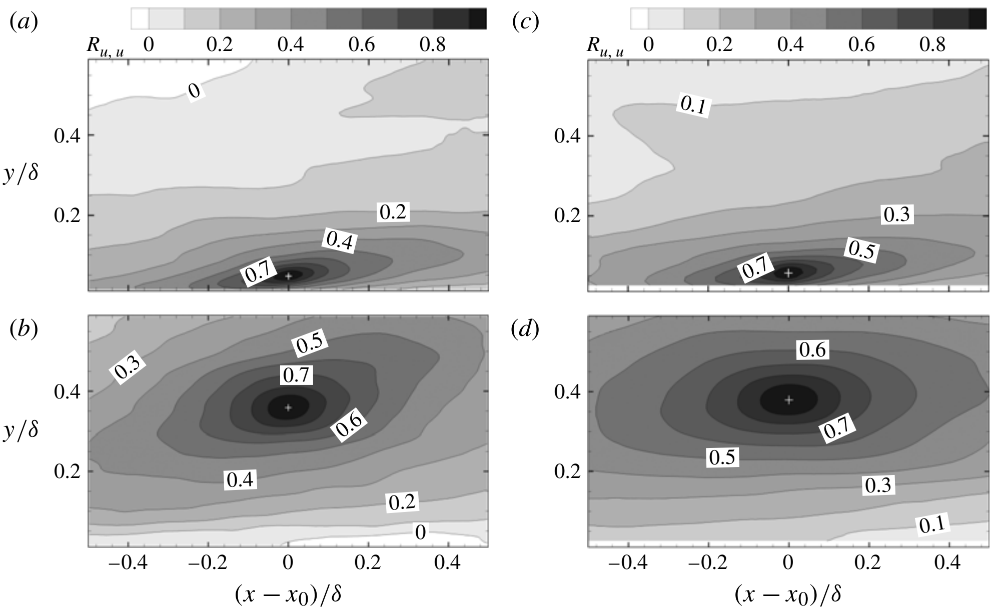

FIGURE 17. Two-point correlations of streamwise velocity fluctuations in the: (*a–b*) ZPG and (*c–d*) FPG boundary layers. Reference elevations are: (*a*) $y_0/\delta = 0.05$, (*b*) 0.36, (*c*) 0.06, (*d*) 0.37. The locations of (x_0, y_0) are denoted by '+'.

Next, we qualitatively explain the differences in inclination of vortices in the near-wall region by comparing their self-induced wall-normal transport to effects of mean velocity gradients. Let us consider an initially horizontal hairpin vortex of characteristic vorticity ω and size r. The vertical self-induced velocity of the vortex head scales as $\Gamma/r \sim \omega r$, where $\Gamma \sim \omega r^2$ is the vortex circulation. Thus, the wall-normal distance travelled by this head in time Δt is $\Delta y \sim [-\omega r + (\partial V/\partial y)\Delta y]\Delta t \sim [-\omega r - (\partial U/\partial x)\Delta y]\Delta t$, accounting for the 2D flow and $\omega < 0$. Further simplification gives $\Delta y \sim (-\omega r \Delta t)/(1 + \partial U/\partial x \Delta t)$. In time Δt, the streamwise distance travelled by the head relative to its base is $\Delta x \sim [(\partial U/\partial x)\Delta x + (\partial U/\partial y)\Delta y]\Delta t$, i.e. $\Delta x \sim (\partial U/\partial y \Delta y \Delta t)/(1 - \partial U/\partial x \Delta t)$. Using the expression for Δy, and further simplification,

Elevation	Mean Δz	Mode Δz	Standard deviation of Δz
ZPG, $y = 1.5$ mm	6.0 mm,	3.8 mm,	3.25 mm,
($y/\delta = 0.06$, $y^+ = 73$)	0.22δ, $290\delta_v$	0.14δ, $184\delta_v$	0.12δ, $157\delta_v$
FPG, $y = 1.5$ mm	5.9 mm,	4.0 mm,	2.73 mm,
($y/\delta = 0.08$, $y^+ = 125$)	0.33δ, $494\delta_v$	0.22δ, $337\delta_v$	0.15δ, $228\delta_v$
ZPG, $y = 4$ mm	7.9 mm,	7.2 mm,	3.06 mm,
($y/\delta = 0.15$, $y^+ = 193$)	0.3δ, $382\delta_v$	0.27δ, $348\delta_v$	0.11δ, $148\delta_v$
FPG, $y = 4$ mm	7.5 mm,	6.8 mm,	3.35 mm,
($y/\delta = 0.22$, $y^+ = 335$)	0.42δ, $624\delta_v$	0.38δ, $567\delta_v$	0.19δ, $280\delta_v$

TABLE 3. Mean, mode values and standard deviations of Δz at different elevations in the ZPG and FPG boundary layers. $Re_\theta(x_1) = 3360$.

the tangent of the vortex inclination angle, β, can be expressed as

$$\tan\beta \approx \frac{1-(\partial U/\partial x)\Delta t}{(\partial U/\partial y)\Delta t}. \tag{5.2}$$

Since, as will be discussed shortly, $|\omega r| \gg (\partial U/\partial x)\Delta y$ for $y/\delta \leqslant 0.2$, $\Delta t \sim -\Delta y/\omega r$. Then, using $\Delta y \sim 0.2\delta$ we obtain,

$$\tan\beta \approx \left[\frac{-\omega r}{0.2\delta(\partial U/\partial y)}\right]\left[1-(\partial U/\partial x)\left(\frac{0.2\delta}{-\omega r}\right)\right]. \tag{5.3}$$

In this equation, the terms in the first and second square brackets compare the effects of $\partial U/\partial y$ and $\partial U/\partial x$, respectively, to the vortex self-induced velocity, indicating that both have an impact on structure inclination. Using procedures described below, for prograde vortices ($\omega < 0$), the mean values of $|\omega r|$ at $y/\delta \leqslant 0.2$ are 0.12 and 0.15 in the ZPG and FPG boundary layers, respectively. Using vertically averaged values of $\partial U/\partial y$ for $y/\delta \leqslant 0.2$, one obtains $(\partial U/\partial y)_{ZPG}/(\partial U/\partial y)_{FPG} \sim 0.54$, and $(\tan\beta)_{ZPG}/(\tan\beta)_{FPG} \sim 1.7$. Thus, the shallower inclination angles in FPG boundary layers should be expected. Experimentally, we obtain a ratio of ~1.5, by visually fitting straight lines to $R_{u,u}$ contours in figures 17(*a*) and 17(*c*). While prograde vortices are likely the heads of hairpin structures (Adrian 2007), retrograde vortices ($\omega > 0$) observed in proximity to prograde ones are presumed to be the signatures of dissecting the same hairpin structures at different locations, or of vortex ring-like structures (Natrajan, Wu & Christensen 2007). They could also result from the interaction of prograde vortices with the wall (Panton 2001). If the analysis is repeated based on the retrograde vortices, the values of $|\omega r|$ at $y/\delta \leqslant 0.2$ are 0.056 and 0.061, and $(\tan\beta)_{ZPG}/(\tan\beta)_{FPG} \sim 2.3$. The substantially lower values of $|\omega r|$ for $\omega > 0$ in comparison to those for $\omega < 0$, consistent with previous observations for swirling strengths (Wu & Christensen 2006), suggest that at least a fraction of the retrograde vortices is not part of hairpin structures.

To obtain ωr, following Wu *et al.* (2011), we identify vortex centres by the local maxima of swirling strength (Zhou *et al.* 1999) within crests of $|\omega|$. The boundary of the vortex is selected as the location where $|\omega|$ decreases to 1/e of its centre value, or the crest edge, if the magnitude does not fall below this threshold. Then, taking ω as the spatially averaged vorticity, and $r = (\text{area}/\pi)^{0.5}$, figure 18 shows PDFs of ωr at $y/\delta \leqslant 0.2$. For both positive and negative vortices, the un-scaled $|\omega r|$ in the FPG boundary layer is higher than that in the ZPG domain (figure 18*a*). However, when scaled by $U_0(x)$, the ZPG values are higher. The results also confirm that $|\omega r| \gg (\partial U/\partial x)\Delta y$ (table 2).

Contours of $R_{p,p}$, shown in figure 19, are oriented almost vertically, with inclinations that are intermediate to those of $R_{u,u}$ and $R_{v,v}$. Contours for the latter (not shown) appear to be nearly circular, similar to previously published results (e.g. Liu, Adrian & Hanratty 2001). Values of $R_{p,p}$ decrease faster upstream of the reference point, especially for the near-wall y_0, similar to the results of Kim (1989) and Tsuji *et al.* (2007). The $R_{p,p}$ length scales are in general closer to those of $R_{v,v}$ than those of $R_{u,u}$, consistent with the fact that $R_{p,v}$ peaks (figure 20) are significantly higher than those of $R_{p,u}$ (not shown). These observations, along with trends depicted in figure 19, suggest that like $R_{v,v}$, $R_{p,p}$ is predominantly affected by characteristic boundary layer vortical structures of size ~0.1 δ. In general, the normalized $R_{p,p}$ length scales in the ZPG boundary layer are shorter than those in the FPG domain. The present ZPG

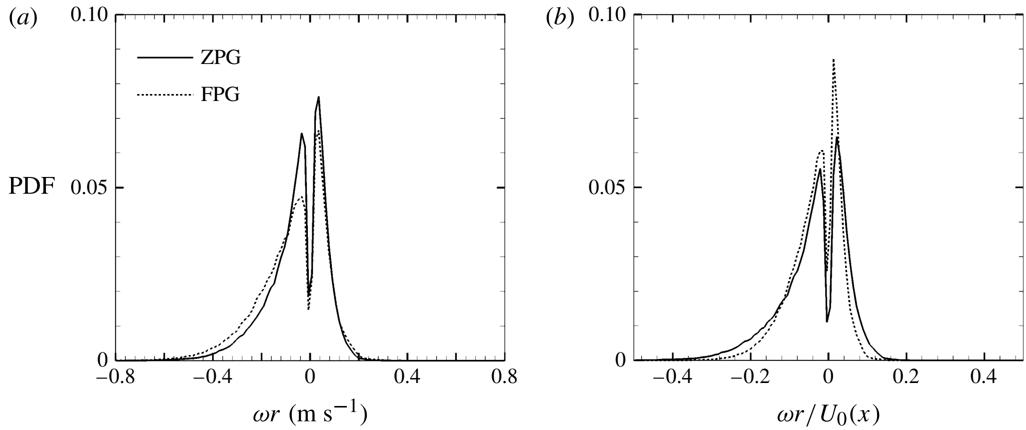

FIGURE 18. PDFs of ωr for $y/\delta \leqslant 0.2$.

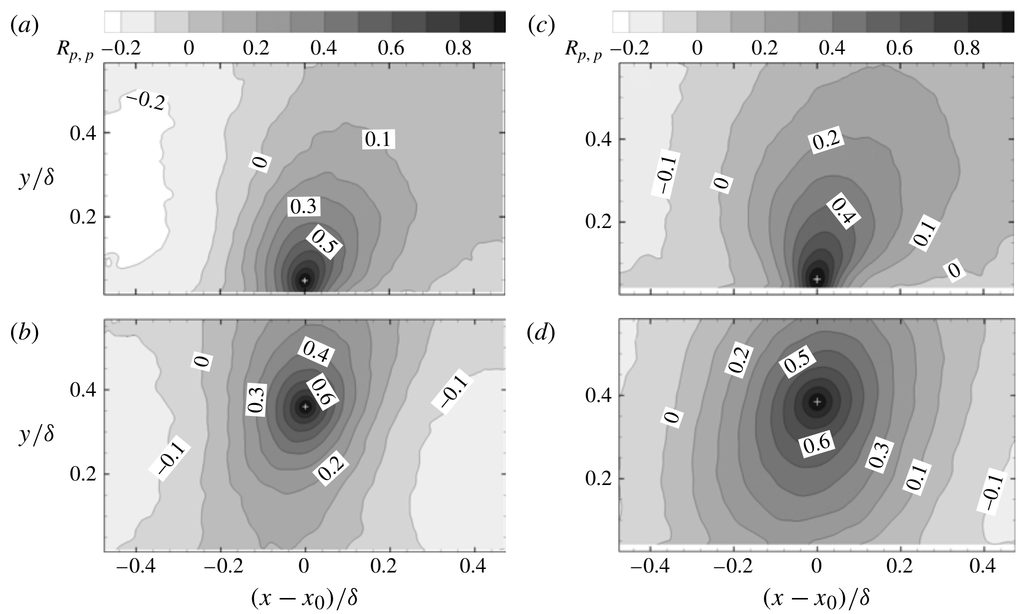

FIGURE 19. Two-point correlations of $p' - p'_{ref}$ in the (*a*–*b*) ZPG and (*c*–*d*) FPG boundary layers. Reference elevations are: (*a*) $y_0/\delta = 0.05$, (*b*) 0.36, (*c*) 0.06, (*d*) 0.37.

length scale for $R_{p,p} = 0$ and $y_0/\delta = 0.05$, $\sim 0.2\,\delta$, is smaller than previous results ($\sim 0.5\,\delta$) based on wall pressure (e.g. Bull 1967; Choi & Moin 1990). However, the differences are smaller for $R_{p,p} = 0.5$, for which the corresponding values are $0.05\,\delta$ and 0.05–$0.2\,\delta$. It is likely that the present $R_{p,p}$ close to the sample area edges is affected by the spatial high-pass filtering caused by subtracting p'_{ref} from p'.

Sample distributions of $R_{p,v}$ (figure 20) indicate that the peaks of p' and v' are displaced. In the ZPG boundary layer (figure 20*a*), the 'lobes' are aligned horizontally, in agreement with prior data based on wall pressure in, e.g. Panton *et al.* (1980) and Kobashi & Ichijo (1986). A possible explanation for this trend, following Thomas &

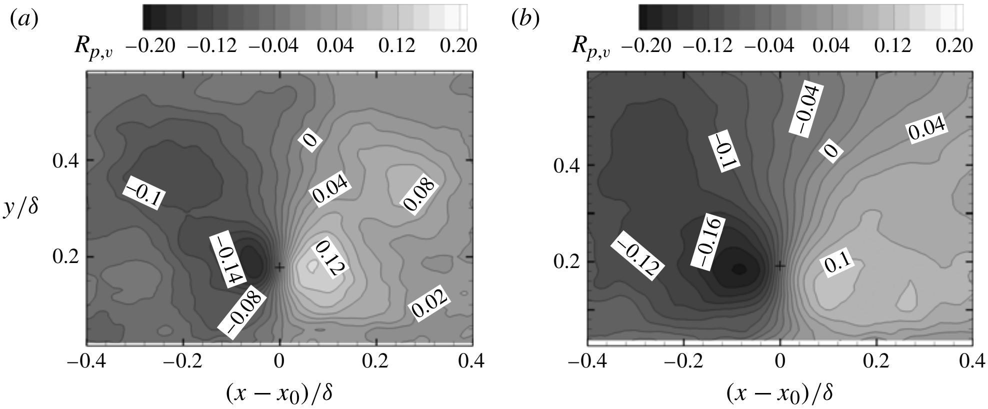

FIGURE 20. Contours for two-point correlations between (*a*) $p' - p'_{ref}(y_0/\delta = 0.18)$ and v' in the ZPG boundary layer and (*b*) $p' - p'_{ref}$ $(y_0/\delta = 0.19)$ and v' in the FPG boundary layer.

Bull (1983), involves the integral of the Poisson equation,

$$p'(\boldsymbol{x}) = \frac{\rho}{2\pi} \int_{\forall} \frac{1}{|\boldsymbol{x} - \boldsymbol{x}'|} \left[2 \frac{\partial U_i}{\partial x_j} \frac{\partial u'_j}{\partial x_i} + \frac{\partial^2}{\partial x_i \partial x_j} (u'_i u'_j - \langle u'_i u'_j \rangle) \right] d\forall(\boldsymbol{x}') \tag{5.4}$$

where the contribution from surface integrals has been neglected. The term $2(\partial U/\partial y)\partial v'/\partial x$, which denotes the interaction between turbulence and mean shear, contributes to $p' > 0$ when $\partial v'/\partial x > 0$, and vice versa, favouring the experimental distribution. For $\partial V/\partial y < 0$ in the FPG boundary layer, a negative $\partial v'/\partial y$ would increase p'. Consequently, the lobes are inclined, reflecting the contributions of both $(\partial U/\partial y)\partial v'/\partial x$ and $(\partial V/\partial y)\partial v'/\partial y$. Interestingly, the 'fast' terms in (5.4) are significantly smaller than the corresponding 'slow' terms (e.g. less than 20 % at $y/\delta = 0.18$ in the ZPG case), with the difference increasing with elevation (not shown). This trend agrees qualitatively with the results of Kim (1989) and Jiménez & Hoyas (2008). However, the slow terms do not seem to contribute significantly to $R_{p,v}$. The inclinations of the lobes do not vary substantially, but the size and spacing between them increase with elevation (not shown), as the size of the turbulent structures increases with distance from the wall. Contours of $R_{\partial p/\partial x,v}$ (figure 21) are noticeably elongated in the vertical direction. In general, $\partial p'/\partial x$ is negatively correlated with v', with peak values falling in the −0.14 to −0.20 range near (x_0, y_0). A negative correlation should be expected in a shear flow, since fluid moving downward would decelerate $(\partial p'/\partial x > 0)$ and vice versa. The peak values of $R_{\partial p/\partial x,u}$ (not shown) are negligible.

6. Flow structures associated with large-scale pressure gradient fluctuations

6.1. *Quadrant analysis and time correlations*

In this section, we explore the impact of strong large-scale pressure gradient fluctuations, $\partial \widetilde{p'}/\partial x$, on turbulence. This investigation is motivated in part by recent studies e.g. Mathis *et al.* (2009) and Hutchins *et al.* (2011), which show that outer layer large-scale velocity impacts the near-wall small-scale turbulence. To obtain

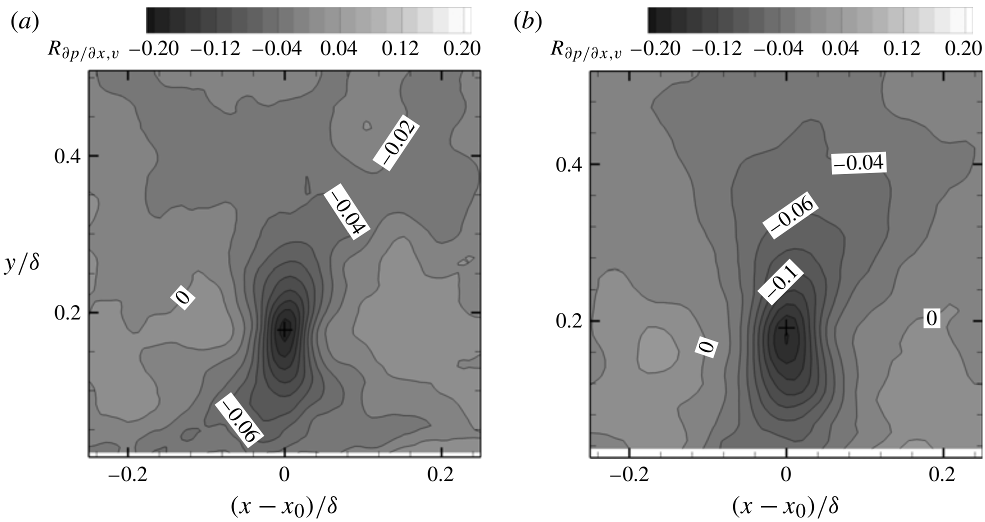

FIGURE 21. Contours for two-point correlations between (*a*) $\partial p'/\partial x(y_0/\delta=0.18)$ and v' in the ZPG boundary layer and (*b*) $\partial p'/\partial x(y_0/\delta=0.19)$ and v' in the FPG boundary layer.

$\partial\widetilde{p'}/\partial x$, we filter $\partial p'/\partial x$ in the same manner as $\widetilde{u'}$ (§ 4). Since Hutchins & Marusic (2007) and Ganapathisubramani *et al.* (2012) show that $T_B U_0/\delta \sim 1$–2 effectively separates the large- and small-scale velocity fluctuations, we choose $T_B U_0/\delta = 1.5$. The same T_B is used to extract $\widetilde{u'}$ and $\partial\widetilde{p'}/\partial x$, following Thomas & Bull (1983). We have also confirmed that results obtained by using $T_B = 6\delta/U_0$ are qualitatively similar to those calculated with $T_B = 1.5\delta/U_0$, i.e. the filter scale is not a critical issue. A strong $\partial\widetilde{p'}/\partial x$ event is defined as one with magnitude greater than its standard deviation, $\sigma_{\partial\widetilde{p}/\partial x}$, which represents ∼30 % of the data. Since the out-of-plane contribution to material acceleration is stronger close to the wall, as a basis for conditional sampling, we use $\partial\widetilde{p'}/\partial x$ at elevations slightly above the logarithmic regions, $y/\delta=0.18$ and 0.19 for the ZPG and FPG cases, respectively. As an initial step, we use time correlations,

$$\gamma_{\varphi,\psi}(y_1, y_2, \tau) = \langle\varphi'(y_1, t).\psi'(y_2, t+\tau)\rangle/[\sigma_\varphi(y_1).\sigma_\psi(y_2)] \tag{6.1}$$

to examine the coherence among $\partial\widetilde{p'}/\partial x$ at different elevations. As figure 22 shows, $\partial\widetilde{p'}/\partial x$ is highly correlated with negligible phase lag across the ZPG boundary layer, with $\gamma_{\partial\widetilde{p}/\partial x,\partial\widetilde{p}/\partial x} > 0.8$ at $\tau=0$ when $y/\delta=0.18$ is involved, justifying our choice of sampling elevation. The characteristic time scale of $\partial\widetilde{p'}/\partial x$, based on τ for which $\gamma_{\partial\widetilde{p}/\partial x,\partial\widetilde{p}/\partial x}$ decays to zero, is clearly dictated by the filter. The same trends and almost the same correlation magnitudes exist in the FPG boundary layer (not shown). Accordingly, our analysis indicates that the results remain largely unchanged for a different choice of sampling elevation.

Figures 23(*a*)–(*d*) compare PDFs of u' and v' at $y/\delta < 0.15$, conditioned on strong $\partial\widetilde{p'}/\partial x$ events. In conformity with the trends for $R_{\partial p/\partial x,v}$, the majority of sweeps occur when $\partial\widetilde{p'}/\partial x > \sigma_{\partial\widetilde{p}/\partial x}$, while most ejections occur during $\partial\widetilde{p'}/\partial x < -\sigma_{\partial\widetilde{p}/\partial x}$. Although they are less distinct, the same trends persist in the FPG domain. Almost all the contribution to these preferred quadrants comes from the large-scale velocity

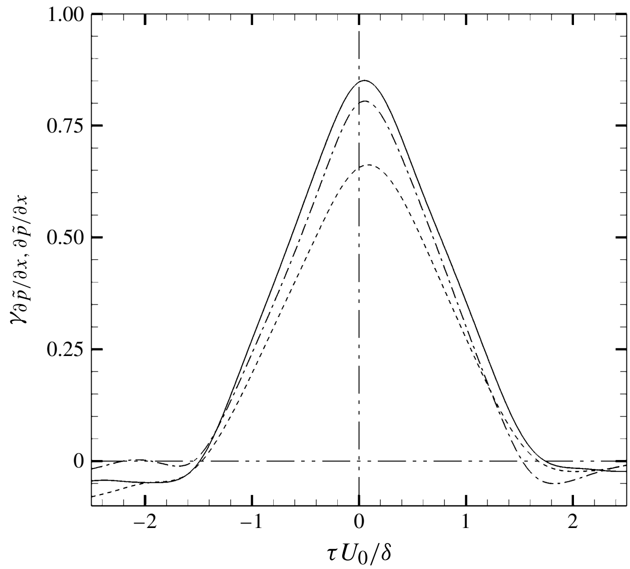

FIGURE 22. Time correlations among $\partial\widetilde{p'}/\partial x$ at different y/δ in the ZPG boundary layer. ———, $\gamma_{\partial\widetilde{p}/\partial x,\partial\widetilde{p}/\partial x}(y_1/\delta = 0.36, y_2/\delta = 0.18, \tau)$; - - - - - -, $\gamma_{\partial\widetilde{p}/\partial x,\partial\widetilde{p}/\partial x}(y_1/\delta = 0.36, y_2/\delta = 0.05, \tau)$; — · — · —, $\gamma_{\partial\widetilde{p}/\partial x,\partial\widetilde{p}/\partial x}(y_1/\delta = 0.18, y_2/\delta = 0.05, \tau)$.

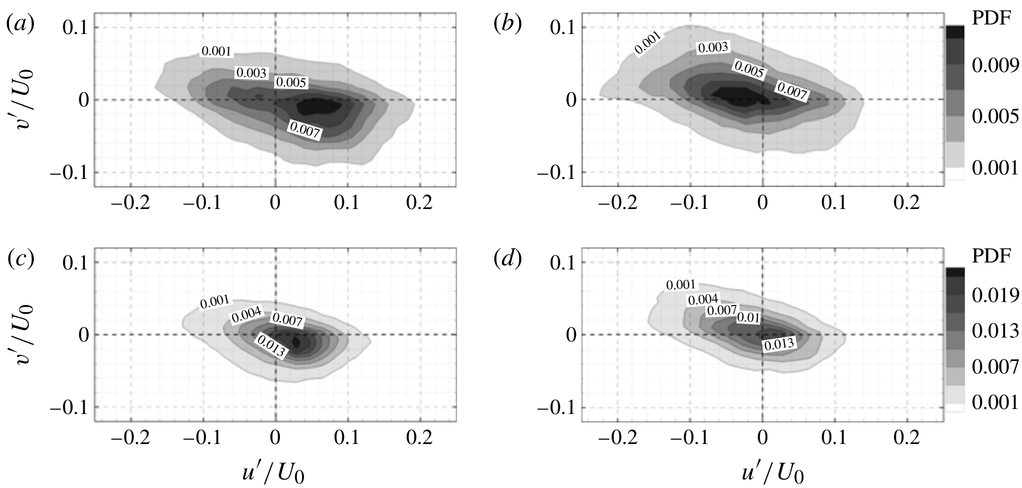

FIGURE 23. PDF of $(u'/U_0,\ v'/U_0)$ at $y/\delta < 0.15$ for (*a* and *c*) $\partial\widetilde{p'}/\partial x > \sigma_{\partial\widetilde{p}/\partial x}$ and (*b* and *d*) $\partial\widetilde{p'}/\partial x < -\sigma_{\partial\widetilde{p}/\partial x}$, sampled at (*a* and *b*) $y/\delta = 0.18$ in the ZPG boundary layer and (*c* and *d*) $y/\delta = 0.19$ in the FPG boundary layer.

fluctuations $(\widetilde{u'}, \widetilde{v'})$, the PDFs of which (figures 24*a*–*d*) show much more pronounced trends in comparison to the unfiltered velocity. Note that the FPG sweeps for $\partial\widetilde{p'}/\partial x > \sigma_{\partial\widetilde{p}/\partial x}$ in figure 24(*c*) are weaker in comparison to those in the ZPG domain (figure 24*a*), in agreement with the characteristics of FPG boundary layers in general (e.g. Bourassa & Thomas 2009). In contrast, for $\partial\widetilde{p'}/\partial x < -\sigma_{\partial\widetilde{p}/\partial x}$, the

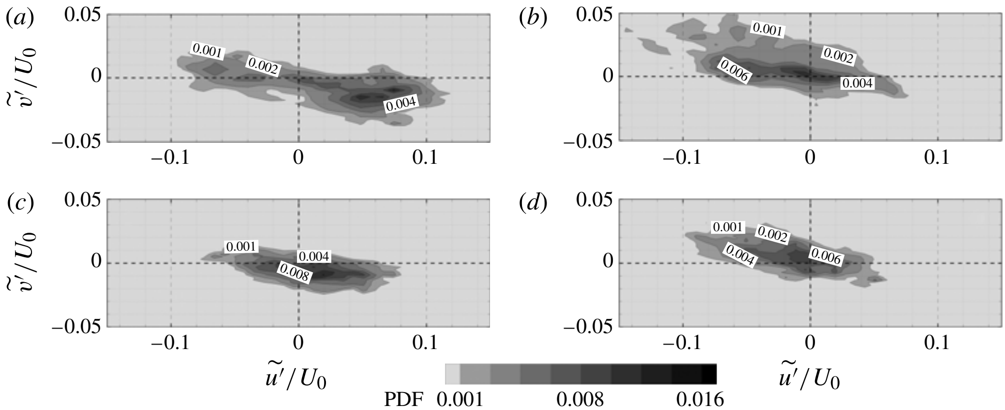

FIGURE 24. PDF of $(\widetilde{u}'/U_0,\ \widetilde{v}'/U_0)$ at $y/\delta < 0.15$ for (*a* and *c*) $\partial\widetilde{p}'/\partial x > \sigma_{\partial\widetilde{p}/\partial x}$ and (*b* and *d*) $\partial\widetilde{p}'/\partial x < -\sigma_{\partial\widetilde{p}/\partial x}$ sampled at (*a* and *b*) $y/\delta = 0.18$ in the ZPG boundary layer and (*c* and *d*) $y/\delta = 0.19$ in the FPG boundary layer.

difference between strengths of ejections in ZPG and FPG flows is small. The PDFs for small-scale fluctuations, $(\widehat{u}',\ \widehat{v}') = (u',\ v') - (\widetilde{u}',\ \widetilde{v}')$, show no marked differences between trends corresponding to favourable or adverse $\partial\widetilde{p}'/\partial x$ (figures not presented). Thus, the preferred quadrants are limited to large-scale flow structures. In the FPG boundary layer, small-scale structures remain largely confined to the near-wall region, and in general make greater contribution to turbulence. Consequently, in figures 23(*c*),(*d*), the trends are less pronounced than those for the ZPG case. As noted before, the results demonstrated in figures 23 and 24 should be expected. Although correlations do not necessarily indicate causality, a downward flow should be typically associated with slowdown of fluid elements, i.e. negative material acceleration and positive streamwise pressure gradient. Conversely, low-momentum fluid advected upward as part of an ejection is expected to accelerate, i.e. the associated pressure gradient is negative. Before concluding, we should note that the preferred quadrants are also evident, but less pronounced, if we use $\partial\widetilde{p}'/\partial x > 0$ (or<0) as a conditioning base, instead of strong events. Furthermore, repeating the analysis for velocity fluctuations at other elevations exhibits similar trends (not shown).

Figures 25 and 26 show time correlations between strong $\partial\widetilde{p}'/\partial x$ events and $(\widetilde{u}',\ \widetilde{v}')$ at different elevations. Near the wall (figures 25*a*, 26*a*), high correlations with no phase lag exist between $\partial\widetilde{p}'/\partial x > \sigma_{\partial\widetilde{p}/\partial x}$ and $\widetilde{v}' < 0$, and $\partial\widetilde{p}'/\partial x < -\sigma_{\partial\widetilde{p}/\partial x}$ and $\widetilde{v}' > 0$. At higher elevations (e.g. figures 25*b*, 26*b*), $\gamma_{\partial\widetilde{p}/\partial x,\widetilde{v}}(y_1,\ y_2,\ \tau)$ peaks decrease slightly, but still remain at ∼0.5. Clearly, strong $\partial\widetilde{p}'/\partial x$ events are accompanied by vertical motions. However, the values of $\gamma_{\partial\widetilde{p}/\partial x,\widetilde{u}}(y_1,\ y_2,\ \tau)$ are lower, and display considerable variation in magnitude and phase with y_2 and between the two boundary layers. As discussed later, these variations reflect differences in the flow structures associated with strong $\partial\widetilde{p}'/\partial x$. Before concluding, we note that the correlation characteristics in figures 25 and 26 are similar if the analysis is repeated without imposing high pressure gradients, but the magnitudes of the correlations decrease, e.g. peak $\gamma_{\partial\widetilde{p}/\partial x,\widetilde{v}}$ is 0.35. Finally, correlations between $\partial\widetilde{p}'/\partial x$ and $(\widehat{u}',\ \widehat{v}')$ are negligible (not shown).

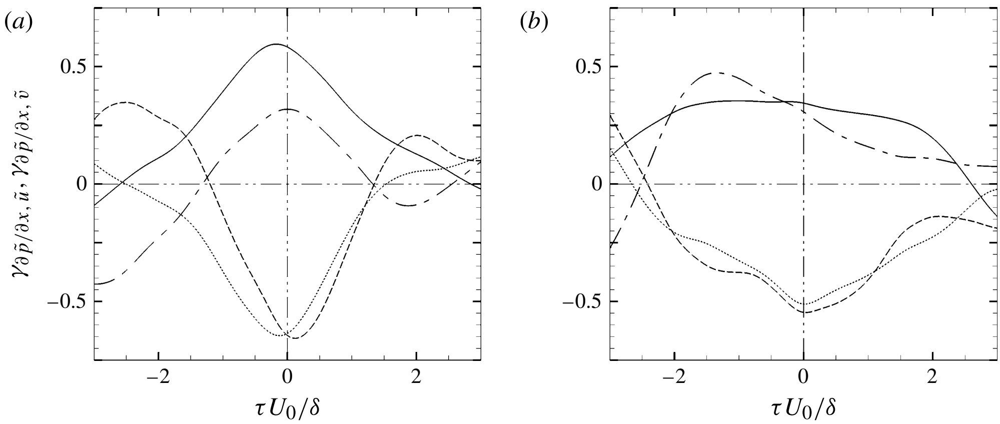

FIGURE 25. Correlation between $\partial\widetilde{p}'/\partial x$ at $y/\delta = 0.18$ and $\widetilde{u}'$, $\widetilde{v}'$ at (*a*) $y/\delta = 0.05$ and (*b*) $y/\delta = 0.18$ in the ZPG boundary layer. — · — · —, $\gamma_{\partial\widetilde{p}/\partial x,\widetilde{u}}|_{\partial\widetilde{p}'/\partial x>\sigma_{\partial\widetilde{p}/\partial x}}$; – – – – – –, $\gamma_{\partial\widetilde{p}/\partial x,\widetilde{v}}|_{\partial\widetilde{p}'/\partial x>\sigma_{\partial\widetilde{p}/\partial x}}$; ———, $\gamma_{\partial\widetilde{p}/\partial x,\widetilde{u}}|_{\partial\widetilde{p}'/\partial x<-\sigma_{\partial\widetilde{p}/\partial x}}$; ··········, $\gamma_{\partial\widetilde{p}/\partial x,\widetilde{v}}|_{\partial\widetilde{p}'/\partial x<-\sigma_{\partial\widetilde{p}/\partial x}}$.

Condition	$Ad+$ $\partial\widetilde{p}'/\partial x > \sigma_{\partial\widetilde{p}/\partial x}$ $\widetilde{u}' > 0$	$Ad-$ $\partial\widetilde{p}'/\partial x > \sigma_{\partial\widetilde{p}/\partial x}$ $\widetilde{u}' < 0$	$Fv-$ $\partial\widetilde{p}'/\partial x < -\sigma_{\partial\widetilde{p}/\partial x}$, $\widetilde{u}' < 0$	$Fv+$ $\partial\widetilde{p}'/\partial x < -\sigma_{\partial\widetilde{p}/\partial x}$, $\widetilde{u}' > 0$
ZPG	0.099	0.051	0.089	0.056
FPG	0.095	0.05	0.099	0.054

TABLE 4. Fraction of data for different pressure gradient and velocity conditions in the ZPG and FPG boundary layers.

6.2. *Conditionally averaged flow structure during adverse pressure gradient fluctuations and sweeps*

To elucidate flow structures characteristic of large-scale pressure gradient fluctuations, we use conditional averaging based on strong $\partial\widetilde{p}'/\partial x$ events. Due to variations in the peak values and phase lags of $\gamma_{\partial\widetilde{p}/\partial x,\widetilde{u}}(y_1, y_2, \tau)$, we further decompose the data for decelerating and accelerating events into periods of $\widetilde{u}' < 0$ and $\widetilde{u}' > 0$ at the sampling points. We provide the fractional contribution of each data subset in table 4, and identify conditions as Ad and Fv for adverse and favourable $\partial\widetilde{p}'/\partial x$, respectively, as well as $+$ and $-$ for the sign of $\widetilde{u}'$. To improve convergence of the conditionally averaged statistics, $\partial\widetilde{p}'/\partial x$ and $\widetilde{u}'$ are sampled at 25 grid points on either side of domain centres, and the corresponding distributions of variables are shifted accordingly before averaging. In the results that follow, overbar indicates conditionally averaged variable, and x' is the streamwise distance from the conditioning point. Figures 27–34 demonstrate the trends for $\partial\widetilde{p}'/\partial x > \sigma_{\partial\widetilde{p}/\partial x}$ and $\widetilde{u}' > 0$ ($Ad+$). Figure 27(*a*) shows contours of $\overline{u'}_{Ad+}$, corresponding streamlines, and a $\overline{\omega'_z}_{Ad+}\delta/U_0$ profile at $x' = 0$ for the ZPG boundary layer. As expected, the flow is dominated by a large-scale sweep. Evidently, $\overline{u'}_{Ad+}$ peaks within a layer that extends diagonally at a shallow angle away from the wall. A growing region of lower, but

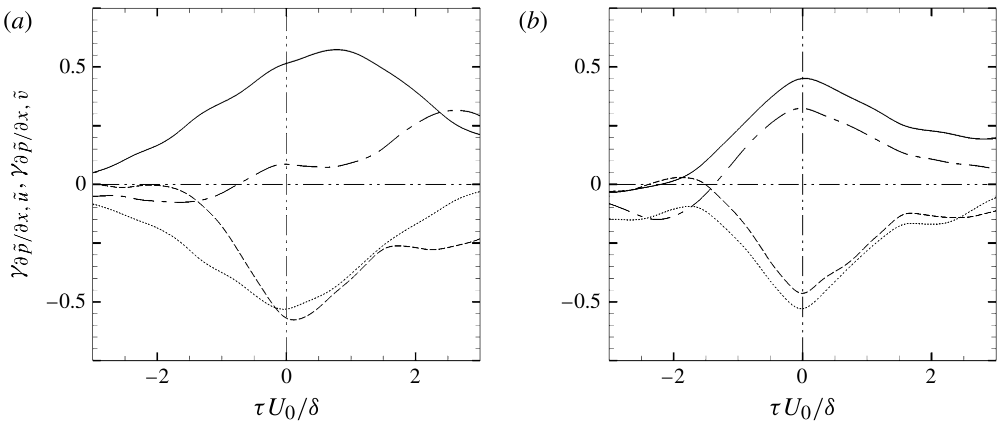

FIGURE 26. Correlation between $\partial\widetilde{p'}/\partial x$ at $y/\delta = 0.19$ and $\widetilde{u'}$, $\widetilde{v'}$ at (a) $y/\delta = 0.06$ and (b) $y/\delta = 0.19$ in the FPG boundary layer. — · — · —, $\gamma_{\partial\tilde{p}/\partial x,\tilde{u}}|_{\partial\widetilde{p'}/\partial x>\sigma_{\partial\tilde{p}/\partial x}}$; - - - - - -, $\gamma_{\partial\tilde{p}/\partial x,\tilde{v}}|_{\partial\widetilde{p'}/\partial x>\sigma_{\partial\tilde{p}/\partial x}}$; ———, $\gamma_{\partial\tilde{p}/\partial x,\tilde{u}}|_{\partial\widetilde{p'}/\partial x<-\sigma_{\partial\tilde{p}/\partial x}}$; ··········, $\gamma_{\partial\tilde{p}/\partial x,\tilde{v}}|_{\partial\widetilde{p'}/\partial x<-\sigma_{\partial\tilde{p}/\partial x}}$.

still positive, $\overline{u'}_{Ad+}$ develops below this layer, where $\overline{\partial u'/\partial x}_{Ad+} < 0$. Close to the wall, $\overline{\omega'_z}_{Ad+}$ becomes positive, presumably due to secondary interaction of the shear layer underneath the peak $\overline{u'}_{Ad+}$ with the wall. Consistent features appear in the corresponding sample instantaneous velocity and vorticity distributions (figure 27b), where very few vortices appear away from the wall, presumably since the sweeping flow suppresses the outward migration of structures. Figure 27(c) shows the $\overline{\partial w'/\partial z}_{Ad+}$ profile at $x' = 0$, calculated using the continuity equation. Its magnitude is negligible at $y/\delta > 0.075$, but becomes positive close to the wall. Thus, as shown in the y–z plane schematic (figure 27c, inset), the conditional mean flow is largely 2D in the outer region, but involves near-wall spanwise stretching as the fluid rushing towards the wall decelerates and migrates out of the x–y plane. Examination of the data shows that the instantaneous large-scale flow is also more 2D in the outer layer. For example, the mean and r.m.s. of $(\partial\widetilde{w'}/\partial z)_{Ad+}(\delta/U_0)$ at $y/\delta > 0.2$ are $\sim$0 and $\sim$0.15, respectively, while the corresponding values at $y/\delta \sim 0.03$ are 0.4 and 0.55. Note that flow symmetry in the schematic is only for illustration.

To examine motions at scales larger than $\sim\delta$, we invoke Taylor's hypothesis and study the evolution of variables in time at the sampling location, with conditions imposed at $t = 0$. Figure 28(a) shows $\overline{\partial\widetilde{p'}/\partial x}_{Ad+}$ contours and $\overline{\partial\widetilde{w'}/\partial z}_{Ad+}$ profiles, while $\overline{\widetilde{u'}}_{Ad+}$ contours and associated streamlines are presented in figure 28(b). The general features of unfiltered velocity, i.e. $\overline{u'}_{Ad+}$, and pressure gradient fluctuations are similar, but noisier, as demonstrated in figure 28(c), indicating that the observed phenomena persist whether we filter the sampled data or not. Caution should be exercised while interpreting these plots, since the advection velocity varies with elevation, and the y axis is stretched relative to $U_0 t$. To assist in interpreting the observed phenomena, figure 29 shows a schematic of the structure inferred from $\overline{\partial\widetilde{w'}/\partial z}_{Ad+}$ and in-plane velocity. Several trends are clearly evident. First, the features around $t = 0$ are consistent with the spatial structures depicted in figure 27. Second, the scales of the educed pressure gradient field are consistent with the filter scale and, in agreement with figure 22, values of $\partial\widetilde{p'}/\partial x$ at all elevations are in phase. Their

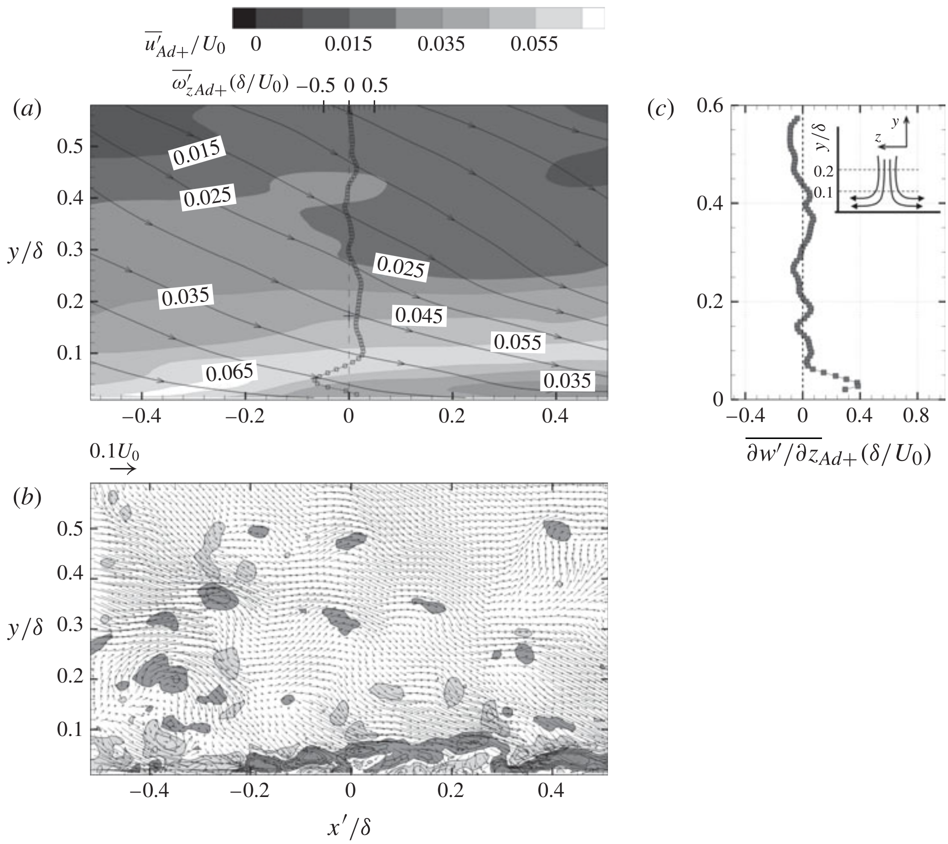

FIGURE 27. Conditionally sampled flow structure in the ZPG boundary layer for $\partial \widetilde{p'}/\partial x > \sigma_{\partial\widetilde{p}/\partial x}$ and $\widetilde{u'} > 0$ ($Ad+$): (a) contours of $\overline{u'}_{Ad+}/U_0$, streamlines and $\overline{\omega'_z}_{Ad+}(\delta/U_0)$ profile at $x'/\delta = 0$; (b) sample snapshot of $\omega'_z\delta/U_0$ and $(u'/U_0,\ v'/U_0)$ vectors; (c) profile of $\overline{\partial w'/\partial z}_{Ad+}(\delta/U_0)$ at $x'/\delta = 0$, with the inset showing the inferred flow structure in the y–z plane. In (b), only alternate vectors are shown; dark grey contours, $\omega'_z\delta/U_0 < -2$; light grey contours, $\omega'_z\delta/U_0 > 2$; contour lines, −11, −8, −5, −2, 2, 5, 8, 11.

magnitudes, however, decrease with increasing y, in agreement with the LES results of Kim (1983). Third, a broad inclined region of sweeping flow coincides with that of $\partial \widetilde{p'}/\partial x > \sigma_{\partial\widetilde{p}/\partial x}$. This domain is preceded in time by an ejection and $\partial \widetilde{p'}/\partial x < 0$, which appear ‘downstream’ of the sampling point. This ejection region expands with ‘distance’ from its origin near the wall. Slightly downstream of the sweep–ejection transition, at $tU_0/\delta \sim -1.1$, the near-wall $\overline{\partial \widetilde{w'}/\partial z}_{Ad+}$ changes from positive to negative, i.e. the flow changes from splatting to anti-splatting.

The results in figures 27–29 indicate that as the outer layer, high-momentum fluid approaches the wall, it loses momentum. Near the wall, around $t = 0$, $\overline{\partial \widetilde{u'}/\partial t}_{Ad+} > 0$ (figure 28b). Of all the convective terms, the dominant one, $\overline{\widetilde{v'\partial U/\partial y}}_{Ad+}$ is approximately equal to $-\overline{\partial \widetilde{u'}/\partial t}_{Ad+}$, and the adverse pressure gradient is balanced by $\overline{\widetilde{u'\partial u'/\partial x}}_{Ad+} < 0$, consistent with figure 27(a). Eventually $\overline{\widetilde{u'}}_{Ad+}$ becomes negative, and ejection starts as part of a phenomenon resembling flow separation. Note that,

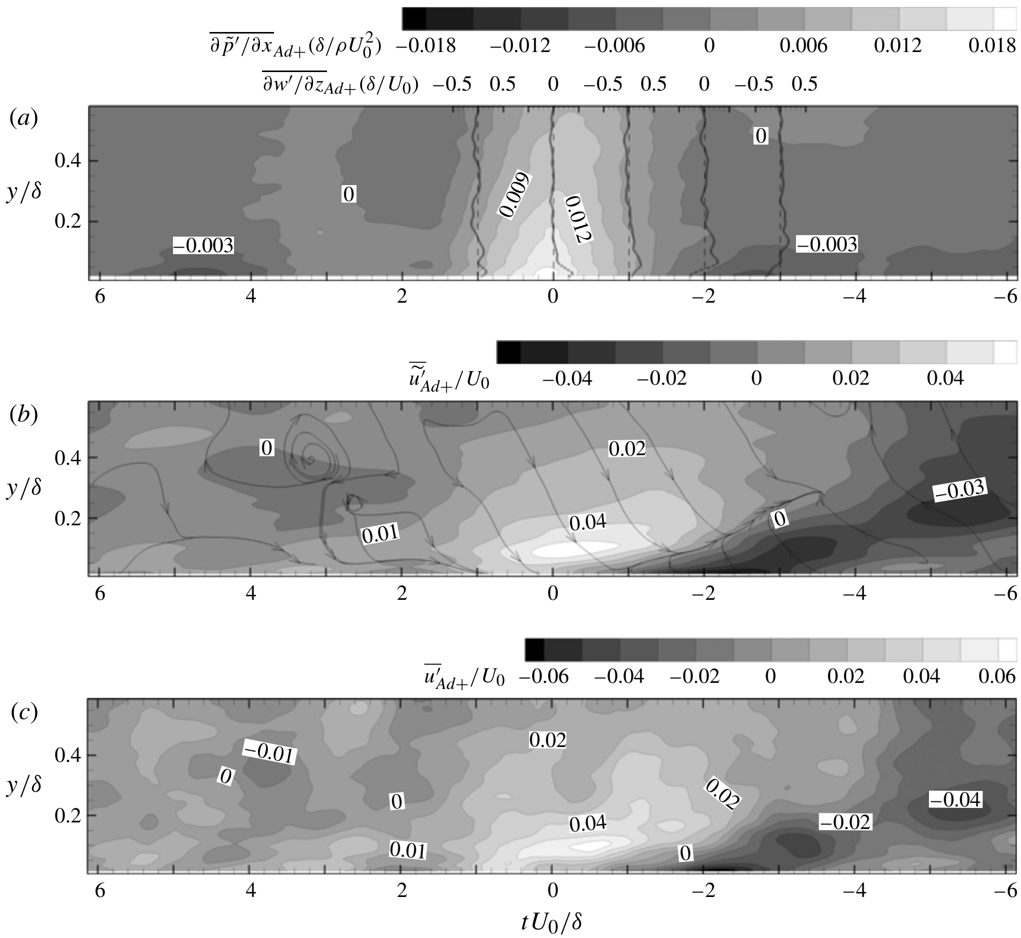

FIGURE 28. Time evolution of the flow structure for $\partial\tilde{p}'/\partial x > \sigma_{\partial\tilde{p}/\partial x}$ and $\tilde{u}' > 0$ ($Ad+$) at ($y/\delta = 0.18$, $t = 0$) in the ZPG boundary layer: (a) contours of $\overline{\partial\tilde{p}'/\partial x}_{Ad+}(\delta/\rho U_0^2)$ and profiles of $\overline{\partial\tilde{w}'/\partial z}_{Ad+}(\delta/U_0)$ at $tU_0/\delta = 1$, 0, −1, −2 and −3; (b) contours of $\overline{\tilde{u}'}_{Ad+}/U_0$ and corresponding streamlines; (c) contours of $\overline{u'}_{Ad+}/U_0$.

accounting for the mean flow, separation does not really occur at our measurement elevations. However, close to the wall, for example, in the viscous sublayer, where fluid has little inertia, adverse pressure gradients should force a flow reversal. Our observations, which do not resolve this region, detect this phenomenon only after it has propagated away from the wall. The transition from near-wall splatting to anti-splatting (figure 29) occurs slightly downstream of the separation point, as the ejected fluid begins to accelerate and the pressure gradient becomes negative. At higher elevations, but still within the ejection, $\overline{\partial\tilde{w}'/\partial z}_{Ad+}$ becomes positive, and peaks just below the sweep–ejection interface. These observations indicate that the large-scale ejection is initiated as a result of adverse pressure gradients associated with impingement of a large-scale sweeping external flow on the wall. These findings agree with the mechanism proposed by Hunt & Morrison (2000) and the observations of Kim (1983, 1985). Although the present flow structure is much larger ($\sim 8000\delta_\nu$

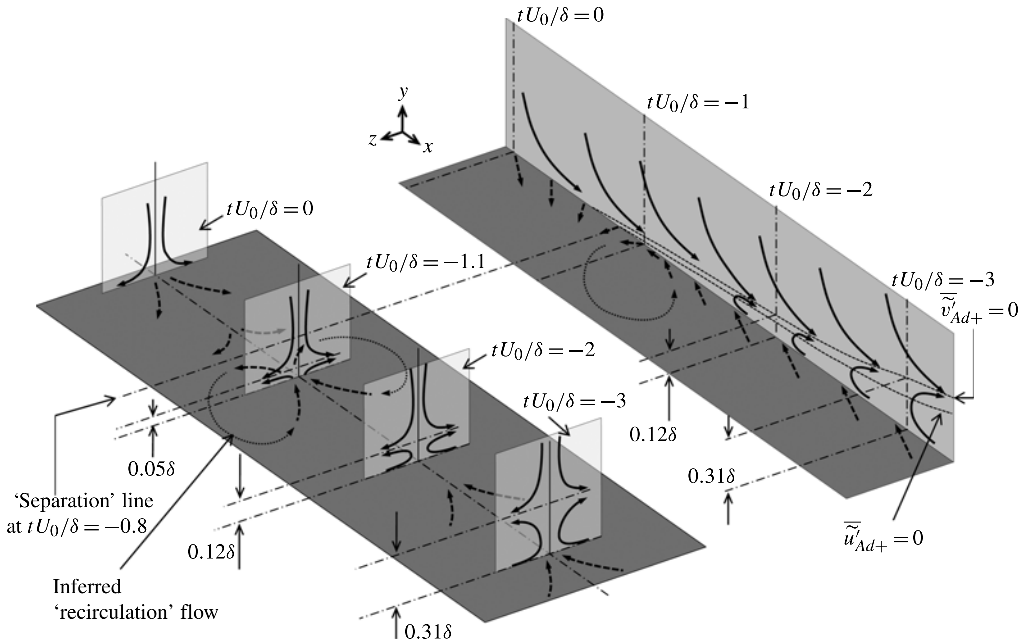

FIGURE 29. Inferred streamlines of velocity fluctuations in x–y (solid lines), y–z (solid lines) and x–z (dashed lines) planes for $\partial\widetilde{p'}/\partial x > \sigma_{\partial\widetilde{p}/\partial x}$ and $\widetilde{u'} > 0$ in the ZPG boundary layer.

long) in comparison to Kim's structures ($\sim 1000\delta_\nu$), the generation and lifting of the streamwise vortices underneath the sweeps, reported by him, agree with the pattern of splatting and anti-splatting motions in figure 29. Similar association of high-pressure fluctuations with inclined shear layers has also been reported previously using wall pressure measurements (e.g. Thomas & Bull 1983), and at much smaller scales in the buffer and lower log regions, in numerical simulations (e.g. Johansson *et al.* 1991; Lo *et al.* 2000). Adverse pressure gradient fluctuations might also be involved in the mechanism causing the abrupt lifting of inner layer vorticity observed by Sheng *et al.* (2009) slightly downstream (20–30δ_ν) of a region with $\partial u'/\partial x < 0$. It should be noted that our results do not identify the origins of these large-scale sweeps. It is possible that such an event is part of a large streamwise-elongated structure, similar to the DNS results of Toh & Itano (2005) or Lozano-Durán, Flores & Jiménez (2012).

Figure 30 presents comparisons of $\overline{u'u'}_{Ad+}$ and $\overline{\widehat{u'}\widehat{u'}}_{Ad+}$ profiles, with their respective ensemble averages, and figure 31 shows similar comparisons for $\overline{u'v'}_{Ad+}$. Near the wall, $\overline{u'u'}_{Ad+}$ increases and $\overline{\widehat{u'}\widehat{u'}}_{Ad+}$ is elevated from $tU_0/\delta = 0$ to -2, i.e. in the region of initiation of ejection underneath sweeps. Further downstream, at $tU_0/\delta = -3$, $\overline{u'u'}_{Ad+}$ returns to its ensemble averaged values, and $\overline{\widehat{u'}\widehat{u'}}_{Ad+}$ decreases to below $\langle\widehat{u'}\widehat{u'}\rangle$. These near-wall trends are consistent with recent observations (e.g. Chung & McKeon 2010; Hutchins *et al.* 2011) that small-scale turbulence peaks downstream of the maximum in large-scale velocity fluctuations ($0 < tU_0/\delta < 0.8$ in figure 28*b*). Small-scale turbulence production, as manifested, for example, by subgrid energy flux (Liu, Katz & Meneveau 1999; Chen, Meneveau & Katz 2006) is expected to increase in regions of $\overline{\partial\widetilde{u'}/\partial x}_{Ad+} < 0$. Further downstream, within the ejection region

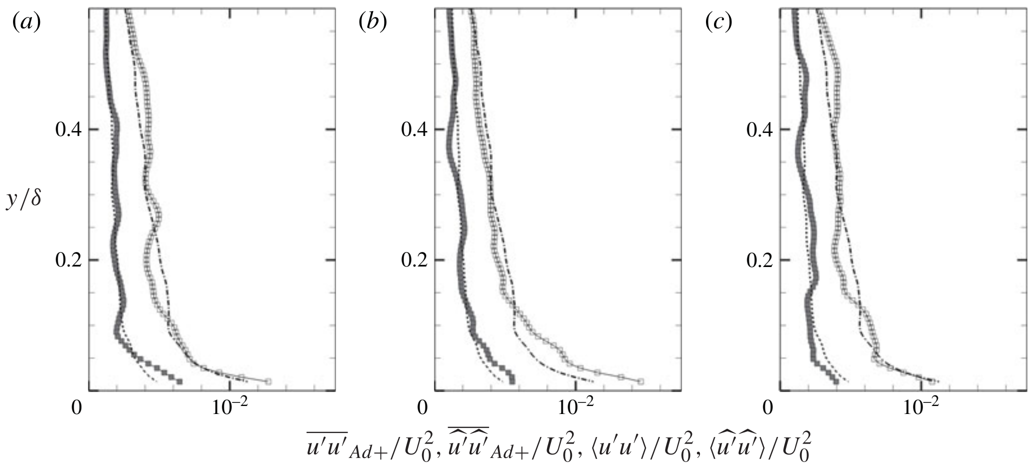

FIGURE 30. Comparisons of the conditionally averaged streamwise velocity fluctuations, $\overline{u'u'}_{Ad+}/U_0^2$ (—⊟—), and their small-scale part, $\overline{\widehat{u'}\widehat{u'}}_{Ad+}/U_0^2$ (—■—), to their ensemble averaged values, $\langle u'u'\rangle/U_0^2$ (– · – · –) and $\langle\widehat{u'}\widehat{u'}\rangle/U_0^2$ (------), respectively, at (*a*) $tU_0/\delta = 0$, (*b*) -2 and (*c*) -3 in the ZPG boundary layer.

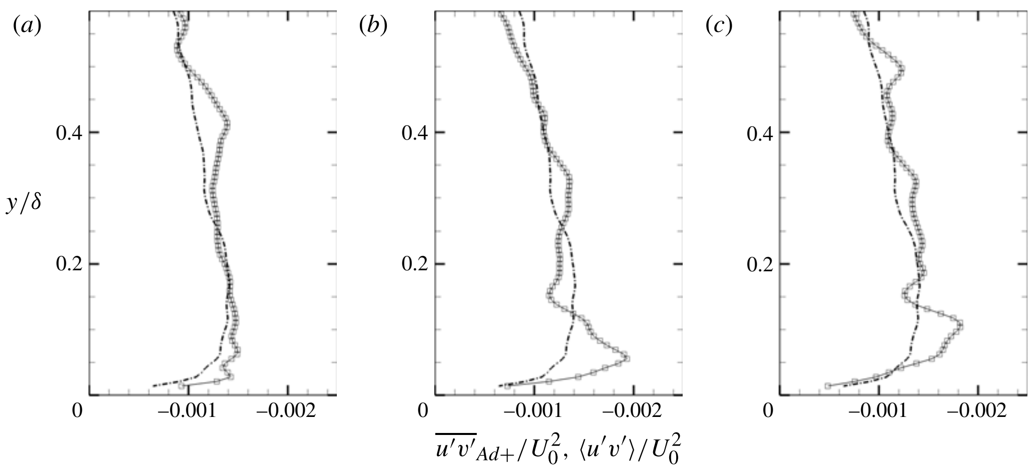

FIGURE 31. Comparison between profiles of $\overline{u'v'}_{Ad+}/U_0^2$ (—⊟—) and $\langle u'v'\rangle/U_0^2$ (– · – · –) at (*a*) $tU_0/\delta = 0$, (*b*) -2 and (*c*) -3 in the ZPG boundary layer.

(e.g. $tU_0/\delta = -3$), $\overline{\widehat{u'}\widehat{u'}}_{Ad+}$ decreases, presumably since $\overline{\partial\widetilde{u'}/\partial x}_{Ad+} > 0$ suppresses small-scale turbulence production. As for $\overline{u'v'}_{Ad+}$ (figure 31), at $tU_0/\delta = 0$, the broad sweeping flow imposes a nearly uniform wall-normal momentum flux all the way to the lowest elevation, where it exceeds $\langle u'v'\rangle$. Further downstream, at $tU_0/\delta = -2$ and -3, $\overline{u'v'}_{Ad+}$ peaks within the growing ejection region.

Spatial contours of $\overline{u'}_{Ad+}$ and profiles of $\overline{\omega'_z}_{Ad+}$ and $\overline{\partial w'/\partial z}_{Ad+}$ in the FPG boundary layer are presented in figure 32. Corresponding instantaneous distributions are similar to those of the ZPG case (not shown). The broad sweeping region, as well as

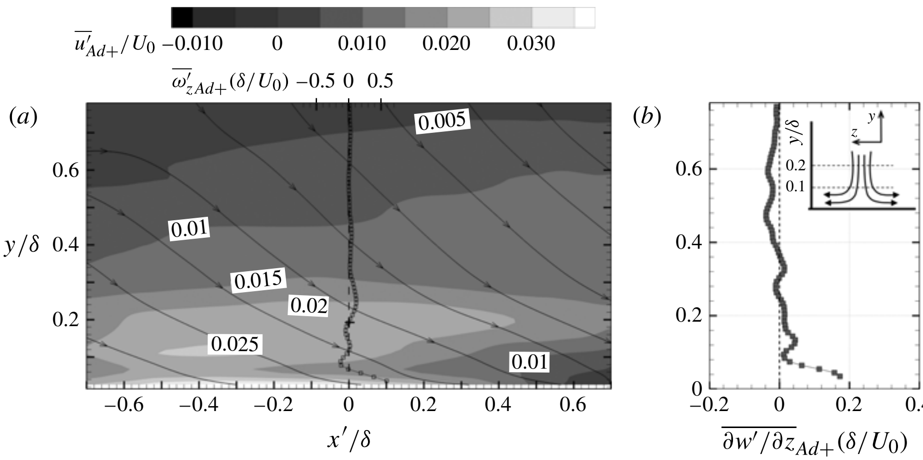

FIGURE 32. Conditionally averaged flow structure in the FPG boundary layer for $\partial\widetilde{p}'/\partial x > \sigma_{\partial\widetilde{p}/\partial x}$ and $\widetilde{u}' > 0$ ($Ad+$): (a) contours of $\overline{u'}_{Ad+}/U_0$, streamlines and $\overline{\omega'_z}_{Ad+}(\delta/U_0)$ profile at $x'/\delta = 0$; (b) profile of $\overline{\partial w'/\partial z}_{Ad+}(\delta/U_0)$ at $x'/\delta = 0$, with the inset showing the inferred flow structure in the y–z plane.

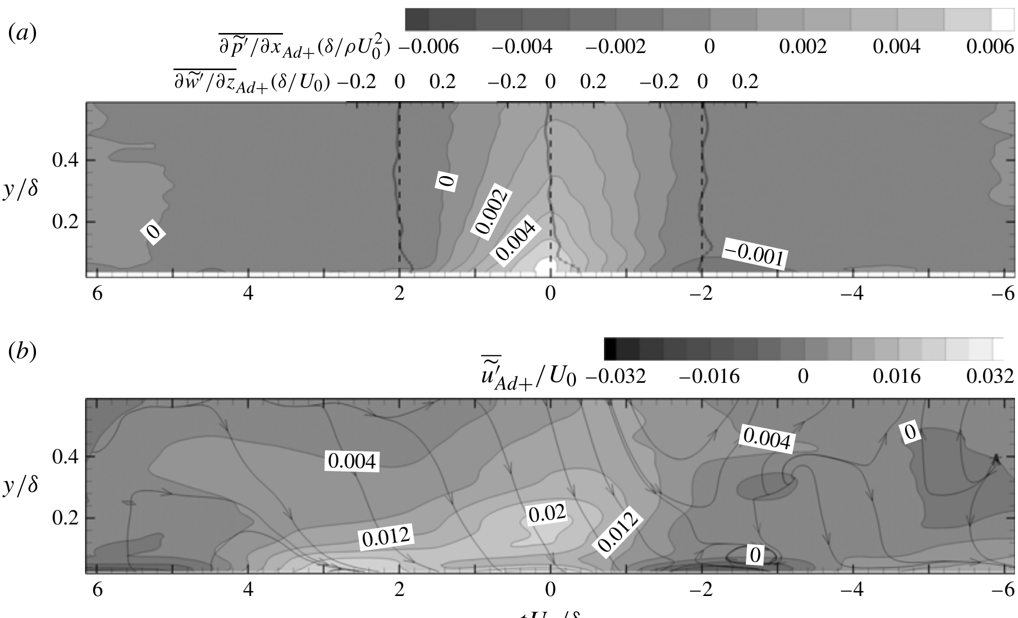

FIGURE 33. Time evolution of the flow structure for $\partial\widetilde{p}'/\partial x > \sigma_{\partial\widetilde{p}/\partial x}$ and $\widetilde{u}' > 0$ ($Ad+$) at ($y/\delta = 0.19$, $t = 0$) in the FPG boundary layer: (a) contours of $\overline{\partial\widetilde{p}'/\partial x}_{Ad+}(\delta/\rho U_0^2)$ and profiles of $\overline{\partial\widetilde{w}'/\partial z}_{Ad+}(\delta/U_0)$ at $tU_0/\delta = 2$, 0 and −2; (b) contours of $\overline{\widetilde{u}'}_{Ad+}/U_0$ and corresponding streamlines.

$\overline{\partial u'/\partial x}_{Ad+} < 0$ and splatting along the wall, are similar to ZPG results. However, $\overline{u'}_{Ad+}$ is weaker, peaks at a higher elevation, and diminishes more rapidly at $x' > 0$.

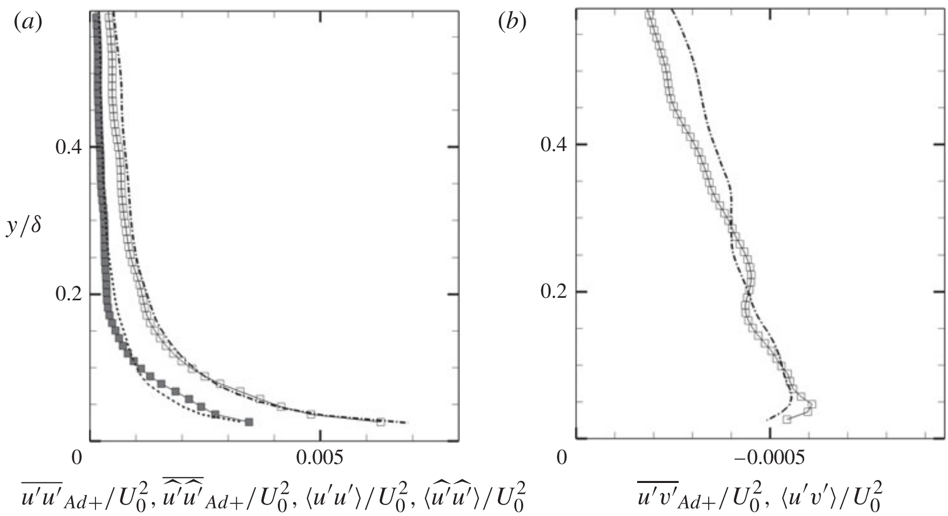

FIGURE 34. Comparisons of (a) the conditionally averaged streamwise velocity fluctuations, $\overline{u'u'}_{Ad+}/U_0^2$ (—□—), and their small-scale part, $\overline{\widehat{u'}\widehat{u'}}_{Ad+}/U_0^2$ (—■—), to their ensemble averaged values, $\langle u'u'\rangle/U_0^2$ (– · – · –) and $\langle \widehat{u'}\widehat{u'}\rangle/U_0^2$ (------), respectively, and (b) $\overline{u'v'}_{Ad+}/U_0^2$ (—□—) to its ensemble averaged values, $\langle u'v'\rangle/U_0^2$ (– · – · –), at $tU_0/\delta = 0$ in the FPG boundary layer.

A consistent picture is depicted in the temporal contours of $\overline{\partial\widetilde{p'}/\partial x}_{Ad+}$ and $\overline{\widetilde{u'}}_{Ad+}$ (figure 33), in which the near-wall, elevated velocity extends far upstream, presumably due to high near-wall shear. Consequently, peak deceleration at the sampling elevation ($y/\delta = 0.19$) occurs near the downstream end of the sweeping region. Accordingly, $\gamma_{\partial\widetilde{p}/\partial x,\widetilde{u}}$ for $y_2 = 0.06\delta$ (figure 26a) shows a time delay of $\sim 2.5\delta$, whereas the ZPG result for $y_2 = 0.05\delta$ (figure 25a) shows a near zero delay. More importantly, unlike the ZPG case, the region of low momentum, $\overline{\partial\widetilde{p'}/\partial x}_{Ad+} < 0$, and anti-splatting for $t < 0$ is extremely narrow and involves very small magnitudes. These trends imply that the mechanism of initiation of ejections by, and downstream of, regions with adverse $\partial\widetilde{p'}/\partial x$ does not play a prominent role in the FPG boundary layer. Accordingly, neither $\overline{u'u'}_{Ad+}$ nor $\overline{\widehat{u'}\widehat{u'}}_{Ad+}$ deviate significantly from their ensemble averaged values (figure 34a). Close to the wall, at $tU_0/\delta = 0$, the magnitude of $\overline{u'v'}_{Ad+}$ is slightly higher than $\langle u'v'\rangle$ (figure 34b), but decreases to levels below it in the weak ejection domain, at $tU_0/\delta = -2$ and -3 (not shown). There are several likely contributors to the suppression of ejection onset downstream of sweeps, and the accompanying weaker momentum transport and small-scale turbulence in the FPG boundary layer. First, the large-scale total pressure gradient ($\partial\widetilde{p}/\partial x$) rarely becomes positive, since the peak $\sigma_{\partial\widetilde{p}/\partial x}/|\partial P/\partial x|$ is 0.14. Thus, the near-wall flow is rarely forced to decelerate and separate to form large-scale ejections. Note, however, that the corresponding ratio for unfiltered fluctuations is 4.1. Thus, flow deceleration occurs commonly at small scales. Second, the outer layer turbulence and associated sweeps are weak in the FPG boundary layer, as is also evident from the PDF in figure 24(c). Since ejections do occur in the FPG region, they seem to be either initiated by other mechanisms, or possibly originate far upstream of the FPG region. The present weak small-scale turbulence underneath sweeps does not agree with the results of Harun $et\ al.$ (2013),

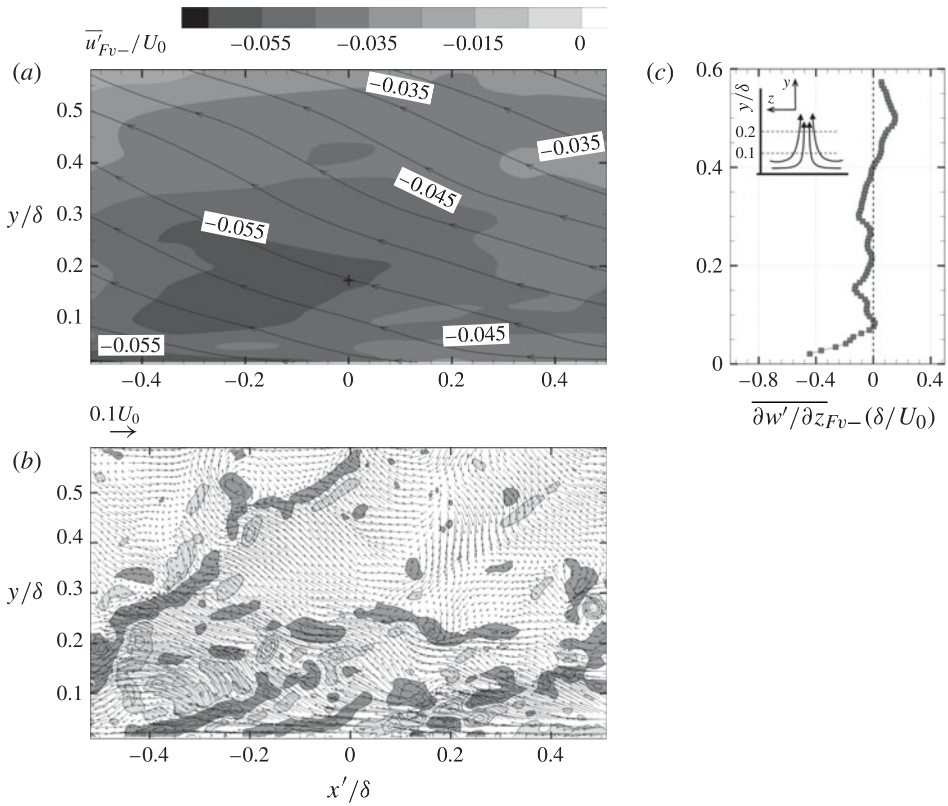

FIGURE 35. Conditionally sampled flow structure in the ZPG boundary layer for $\partial\widetilde{p}'/\partial x < -\sigma_{\partial\widetilde{p}/\partial x}$ and $\widetilde{u}' < 0$ ($Fv-$): (*a*) contours of $\overline{u'}_{Fv-}/U_0$ and streamlines; (*b*) sample snapshot of $\omega_z'\delta/U_0$ and $(u'/U_0,\ v'/U_0)$ vectors; (*c*) profile of $\overline{\partial w'/\partial z}_{Fv-}(\delta/U_0)$ at $x'/\delta = 0$, with the inset showing the inferred flow structure in the y–z plane. In (*b*), only alternative vectors are shown; dark grey contours, $\omega_z'\delta/U_0 < -2$; light grey contours, $\omega_z'\delta/U_0 > 2$; contour lines, −11, −8, −5, −2, 2, 5, 8, 11.

presumably since their K is very small ($\sim 0.08 \times 10^{-6}$), allowing near-wall $\partial\widetilde{p}/\partial x$ to become positive more often.

6.3. *Conditionally averaged flow structure during FPG fluctuations and ejections*

Results for $\partial\widetilde{p}'/\partial x < -\sigma_{\partial\widetilde{p}/\partial x}$ and $\widetilde{u}' < 0$ ($Fv-$) events are presented in figures 35–40. As expected, the spatial $\overline{u'}_{Fv-}$ contours and corresponding streamlines in the ZPG boundary layer (figure 35*a*) show a large-scale ejection. In contrast to the effects of mean FPG, which suppresses the wall-normal transport of coherent structures, the sample snapshot (figure 35*b*) displays trains of vortices propagating away from the wall, transporting small-scale turbulence into the outer layer. As is evident from the $\overline{\partial w'/\partial z}_{Fv-}$ profile (figure 35*c*), and consistent with trends shown in figure 29, ejections involve near-wall anti splatting, but the conditionally averaged (and the instantaneous) flow becomes more two-dimensional in the outer layer. The temporal contours of $\overline{\partial\widetilde{p}'/\partial x}_{Fv-}$ and $\overline{\widetilde{u}'}_{Fv-}$ (figures 36*a*, 36*b*) show that the $\overline{\partial\widetilde{p}'/\partial x}_{Fv-} < 0$ region spans $\sim 6\,\delta$, and that the fluctuations peak at the wall. Upstream of this region, around $tU_0/\delta \sim 4$,

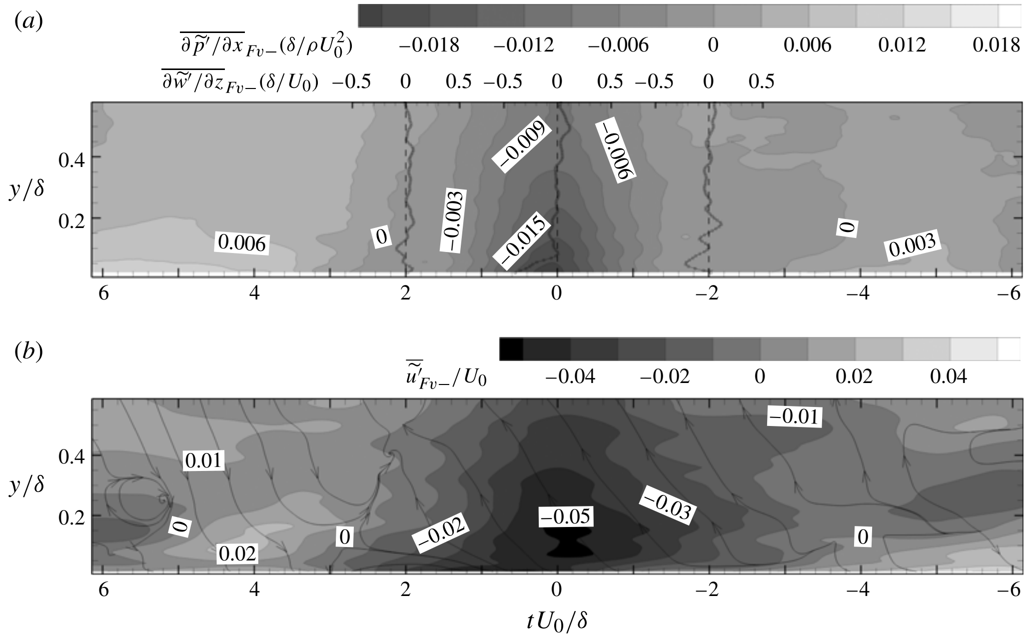

FIGURE 36. Time evolution of the flow structure for $\partial\widetilde{p'}/\partial x < -\sigma_{\partial\widetilde{p}/\partial x}$ and $\widetilde{u'} < 0$ ($Fv-$) at ($y/\delta = 0.18$, $t = 0$) in the ZPG boundary layer: (a) contours of $\overline{\partial\widetilde{p'}/\partial x}_{Fv-}(\delta/\rho U_0^2)$ and profiles of $\overline{\partial\widetilde{w'}/\partial z}_{Fv-}(\delta/U_0)$ at $tU_0/\delta = 2$, 0 and -2; (b) contours of $\widetilde{\overline{u'}}_{Fv-}/U_0$ and corresponding streamlines.

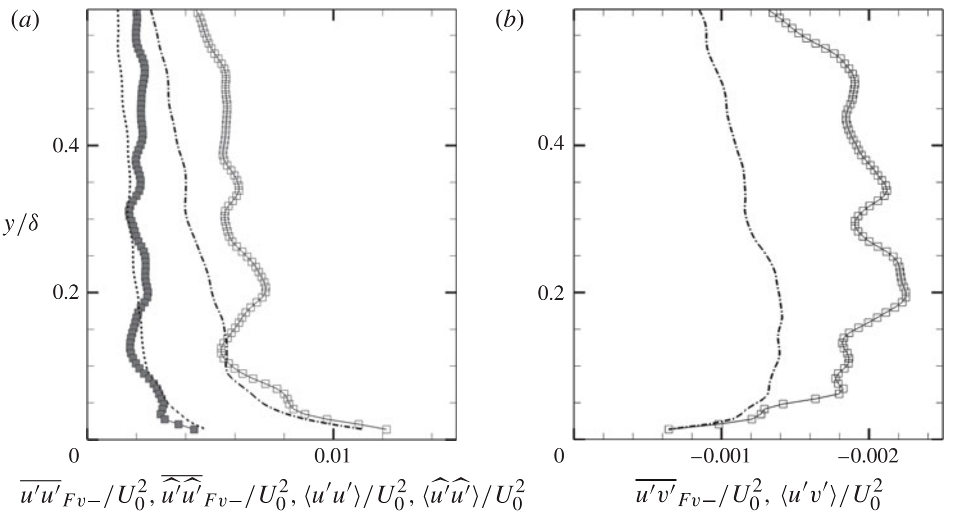

FIGURE 37. Comparisons of (a) the conditionally averaged streamwise velocity fluctuations, $\overline{u'u'}_{Fv-}/U_0^2$ (—□—), and their small-scale part, $\overline{\widehat{u'}\widehat{u'}}_{Fv-}/U_0^2$ (—■—), to their ensemble averaged values, $\langle u'u'\rangle/U_0^2$ (▬ · ▬ · ▬) and $\langle\widehat{u'}\widehat{u'}\rangle/U_0^2$ (▬▬▬▬▬▬), respectively, and (b) $\overline{u'v'}_{Fv-}/U_0^2$ (—□—) to its ensemble averaged values, $\langle u'v'\rangle/U_0^2$ (▬ · ▬ · ▬), at $tU_0/\delta = 0$ in the ZPG boundary layer.

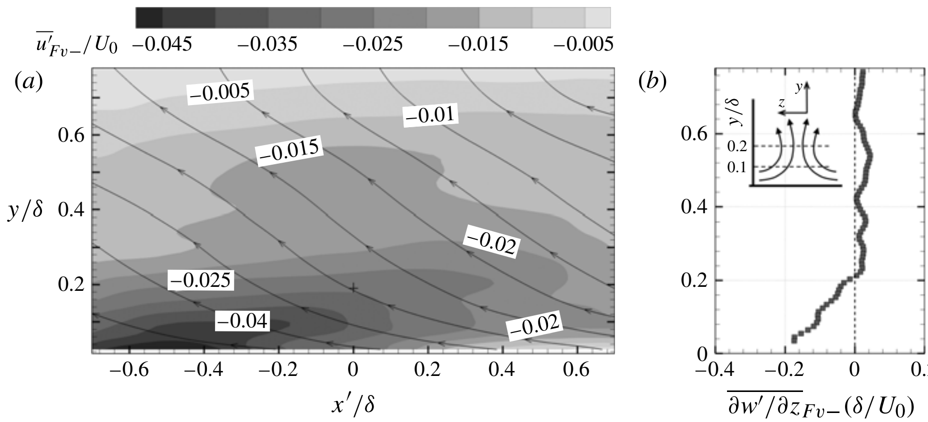

FIGURE 38. Conditionally averaged flow structure in the FPG boundary layer for $\partial\widetilde{p}'/\partial x < -\sigma_{\partial\widetilde{p}/\partial x}$ and $\widetilde{u}' < 0$ ($Fv-$): (a) contours of $\overline{u'}_{Fv-}/U_0$ and streamlines; (b) profile of $\overline{\partial w'/\partial z}_{Fv-}(\delta/U_0)$ at $x'/\delta = 0$, with the inset showing the inferred flow structure in the y–z plane.

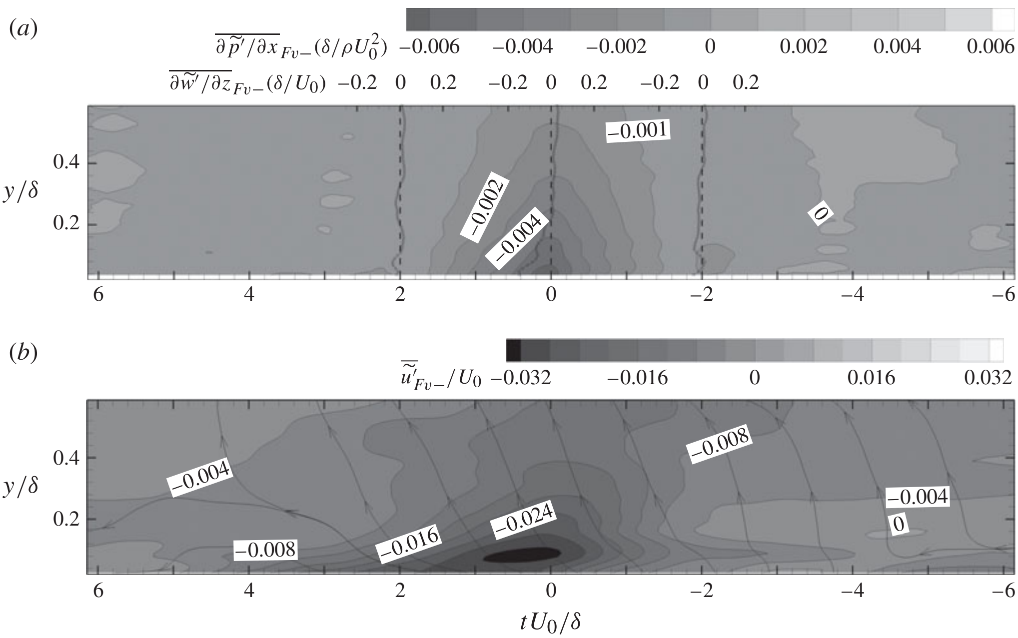

FIGURE 39. Time evolution of the flow structure for $\partial\widetilde{p}'/\partial x < -\sigma_{\partial\widetilde{p}/\partial x}$ and $\widetilde{u}' < 0$ ($Fv-$) at ($y/\delta = 0.19$, $t = 0$) in the FPG boundary layer: (a) contours of $\overline{\partial\widetilde{p}'/\partial x}_{Fv-}(\delta/\rho U_0^2)$ and profiles of $\overline{\partial\widetilde{w}'/\partial z}_{Fv-}(\delta/U_0)$ at $tU_0/\delta = 2$, 0 and −2; (b) contours of $\overline{\widetilde{u}'}_{Fv-}/U_0$ and corresponding streamlines.

there is a weak, but clear, signature of a sweeping flow with $\overline{\partial\widetilde{p}'/\partial x}_{Fv-} > 0$, indicating that at least some of the ejections are preceded by large-scale sweeps, consistent with results in § 6.2. However, the sweep–ejection interface is not as distinct, and does

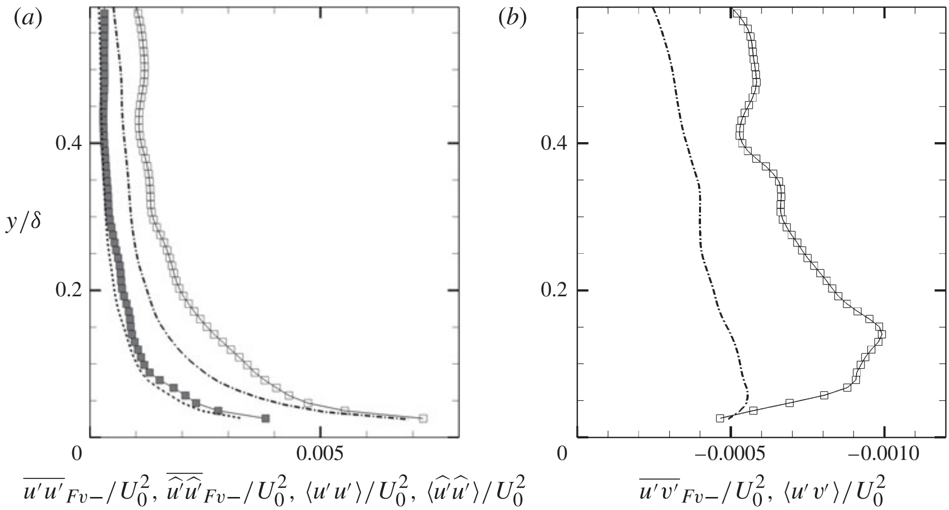

FIGURE 40. Comparisons of (a) the conditionally averaged streamwise velocity fluctuations, $\overline{u'u'}_{Fv-}/U_0^2$ (—□—), and their small-scale part, $\overline{\widehat{u'}\widehat{u'}}_{Fv-}/U_0^2$ (—■—), to their ensemble averaged values, $\langle u'u'\rangle/U_0^2$ (– · – · –) and $\langle\widehat{u'}\widehat{u'}\rangle/U_0^2$ (- - - - - -), respectively, and (b) $\overline{u'v'}_{Fv-}/U_0^2$ (—□—) to its ensemble averaged values, $\langle u'v'\rangle/U_0^2$ (– · – · –), at $tU_0/\delta = 0$ in the FPG boundary layer.

not have the previously shown low inclination angle. This difference might be a conditional sampling artefact or, more likely, occurs because not all ejections are preceded by sweeps, as is indeed revealed by instantaneous data. Sample profiles of $\overline{u'u'}_{Fv-}$, $\overline{\widehat{u'}\widehat{u'}}_{Fv-}$ and $\overline{u'v'}_{Fv-}$ at $t = 0$ (figure 37) show that $\overline{u'u'}_{Fv-}$ is close to $\langle u'u'\rangle$ near the wall, but is significantly higher in the outer region. On the other hand, $\overline{\widehat{u'}\widehat{u'}}_{Fv-}$ is slightly lower than $\langle\widehat{u'}\widehat{u'}\rangle$ near the wall, and slightly higher away from the wall. The latter trends are consistent with those reported in, for example, Hutchins *et al.* (2011). The differences between $\overline{u'u'}_{Fv-}$, and $\overline{\widehat{u'}\widehat{u'}}_{Fv-}$ indicate that the increase in outer layer turbulence during ejections is mostly associated with large-scale motions. Except for very close to the wall, the wall-normal momentum transport (figure 37b) during $Fv-$ events is much higher than $\langle u'v'\rangle$, consistent with figure 31.

Some of the trends for $Fv-$ events in the FPG boundary layer (figures 38–40) are consistent with ZPG results, e.g. the near-wall anti-splatting (figure 38b), as well as high $\overline{u'u'}_{Fv-}$ and $\overline{u'v'}_{Fv-}$ relative to their ensemble averaged values (figures 40a, 40b). There are, however, obvious differences. First, near the wall, ejection extends far upstream ($\sim 4\delta$) of $t = 0$ and the peak in favourable $\overline{\partial\widetilde{p'}/\partial x}_{Fv-}$ (figure 39), consistent with $\gamma_{\partial\widetilde{p}/\partial x,\widetilde{u}}$ (figure 26a). Thus, the $\overline{\partial\widetilde{p'}/\partial x}_{Fv-} < 0$ peak occurs well after the ejection is initiated, i.e. the pressure field is not the cause of the ejection, but might be an outcome of it. Second, the FPG ejections decay rapidly away from the wall, and are quite weak at $y/\delta > 0.3$. Third, in agreement with quadrant analysis, the strength of ejections is much greater than that of sweeps (figures 33b, 39b). Finally, there is no sign of any sweep upstream of the ejection, which also agrees with instantaneous movies. As the samples in figures 14(c) and 15(b) show, the streamwise-elongated ejections are directly associated with very long, nearly horizontal trains of vortices,

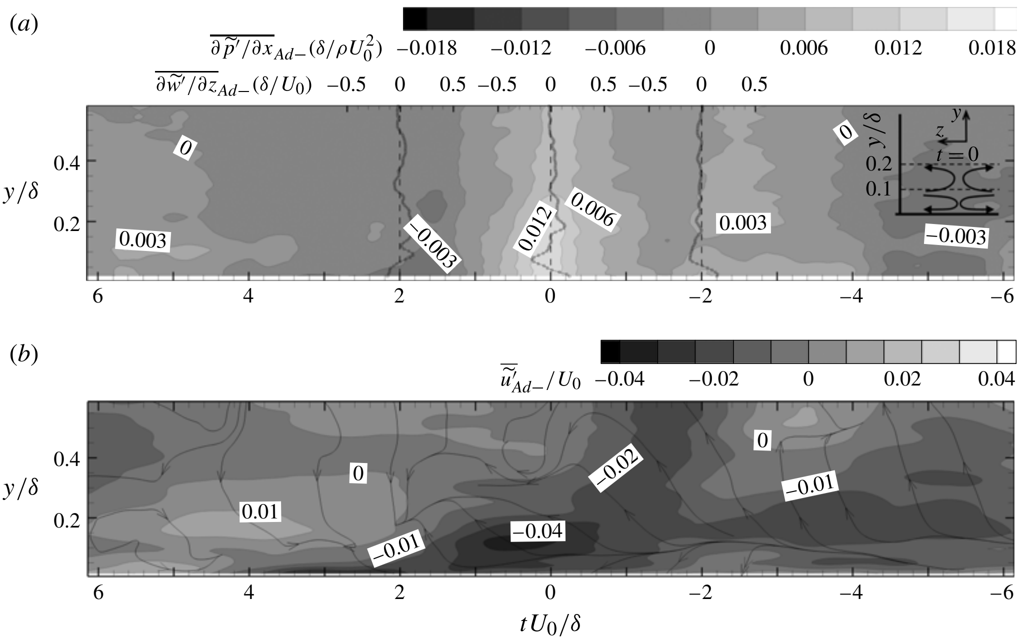

FIGURE 41. Time evolution of the flow structure for $\partial \widetilde{p}'/\partial x > \sigma_{\partial\widetilde{p}/\partial x}$ and $\widetilde{u}' < 0$ ($Ad-$) at ($y/\delta = 0.18$, $t = 0$) in the ZPG boundary layer: (*a*) contours of $\overline{\partial \widetilde{p}'/\partial x}_{Ad-}(\delta/\rho U_0^2)$ and profiles of $\overline{\partial \widetilde{w}'/\partial z}_{Ad-}(\delta/U_0)$ at $tU_0/\delta = 2$, 0 and -2, with the inset showing the inferred flow structure in the y–z plane at $t = 0$; (*b*) contours of $\widetilde{\overline{u}}'_{Ad-}/U_0$ and corresponding streamlines.

which frequently extend axially beyond our field of view, and rarely appear to be linked to sweeping events immediately upstream. As discussed before, ejections are likely to be initiated in the FPG boundary layer by mechanisms other than those involving sweeps and adverse $\partial \widetilde{p}'/\partial x$. It is also possible that many of the ejections originate far upstream, and then sustain themselves, e.g. through autogeneration (Zhou, Adrian & Balachandar 1996; Zhou *et al.* 1999) for a long distance. Such a possibility is also suggested by similar un-scaled widths of the low-speed regions in the ZPG and FPG domains, as discussed in § 4.

6.4. *Conditionally averaged flow structure for the infrequent Ad− and Fv+ events*

Results for the less likely events, $Ad-$ and $Fv+$, are briefly summarized in figures 41 and 42, respectively. We do not show spatially averaged contours since they are consistent with temporal averages. In the ZPG boundary layer, $\overline{\partial \widetilde{p}'/\partial x}_{Ad-}$ (figure 41*a*) is significantly weaker than $\overline{\partial \widetilde{p}'/\partial x}_{Ad+}$ (figure 28*a*). The $\widetilde{\overline{u}}'_{Ad-}$ contours for $t > 0$ are similar to those of $\widetilde{\overline{u}}'_{Ad+}$ for $t < 0$ (figure 28*b*), with the sweep–ejection transition and proper signs of $\partial \widetilde{p}'/\partial x$. However, around $t = 0$, growth of the ejection region seems to be suppressed by $\partial \widetilde{p}'/\partial x > 0$. Below the ejection peak, $\overline{\widetilde{v}'}_{Ad-} < 0$, $\overline{\partial \widetilde{u}'/\partial x}_{Ad-} < 0$ (not shown) and $\overline{\partial \widetilde{w}'/\partial z}_{Ad-} > 0$, as expected for $\partial \widetilde{p}'/\partial x > 0$. Further away from wall, $\overline{\partial \widetilde{w}'/\partial z}_{Ad-}$ changes sign twice, indicating spanwise contraction between extension

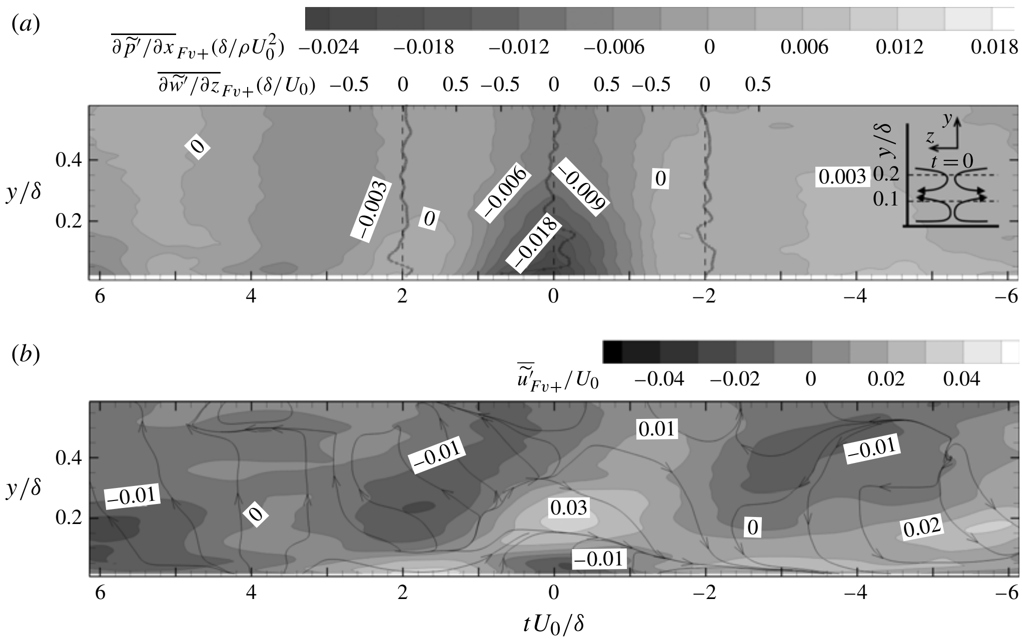

FIGURE 42. Time evolution of the flow structure for $\partial\widetilde{p}'/\partial x < -\sigma_{\partial\widetilde{p}/\partial x}$ and $\widetilde{u}' > 0$ ($Fv+$) at ($y/\delta = 0.18$, $t = 0$) in the ZPG boundary layer: (a) contours of $\overline{\partial\widetilde{p}'/\partial x}_{Fv+}(\delta/\rho U_0^2)$ and profiles of $\overline{\partial\widetilde{w}'/\partial z}_{Fv+}(\delta/U_0)$ at $tU_0/\delta = 2$, 0 and -2, with the inset showing the inferred flow structure in the y–z plane at $t = 0$; (b) contours of $\overline{\widetilde{u}'}_{Fv+}/U_0$ and corresponding streamlines.

domains (figure 41a, inset). The results for the FPG case (not presented) are similar around $t = 0$, but, as expected, the ejection is not preceded by a sweep. Figure 42 shows that peak $\overline{\partial\widetilde{p}'/\partial x}_{Fv+}$ in the ZPG boundary layer is markedly stronger than that of $\overline{\partial\widetilde{p}'/\partial x}_{Fv-}$. Around $t = 0$, the narrow ejection region at $y/\delta < 0.1$ seems to be confined under a sweep. The flow structure away from $t = 0$ is quite complex and does not lend itself to a straightforward interpretation. To explore this flow structure further, 3D measurements would be required. The $\overline{\partial\widetilde{w}'/\partial z}_{Fv+}$ profile at $t = 0$ shows that, consistent with our observations so far, $\partial\widetilde{p}'/\partial x < 0$ is associated with near-wall anti-splatting as the fluid there accelerates. Spanwise extension at the sweep–ejection interface, and contraction above it, are illustrated in the schematic in figure 42(a), which is consistent with the flow pattern observed for $Ad+$ events. The flow structure near $t = 0$ for the FPG case (not shown) is very similar, except, as expected, that the structure is markedly stretched in the streamwise direction.

7. Summary and concluding remarks

We study the effects of mean (favourable) and large-scale fluctuating pressure gradients on boundary layer turbulence. Two-dimensional (2D) PIV measurements have been performed upstream of and within a sink flow, at two inlet Reynolds numbers, $Re_\theta(x_1) = 3360$ and 5285. The corresponding values of K – 1.3×10^{-6} and 0.6×10^{-6} – are well below the relaminarization level. Time-resolved data for $Re_\theta(x_1) = 3360$ enable calculation of instantaneous pressure by integrating the planar projection of material acceleration. The effects of out-of-plane motion on the measurement accuracy are assessed. For this case, we also determine the wall shear stress in the FPG boundary layer using digital holography to measure the velocity profile in the viscous sublayer and buffer layer.

Locally normalized Reynolds stresses in the FPG domain are weaker than those under ZPG conditions. For the higher Reynolds number case, all stresses show a near-wall collapse in the constant K region. However, for both Reynolds numbers, un-scaled stresses in the FPG boundary layer are higher close to the wall and lower away from the wall in comparison to the ZPG domain. This trend is caused by suppression of outward diffusion of newly produced near-wall turbulence. An approximate analysis comparing the self-induced rise velocity of vortical structures to straining by the mean flow shows that this confinement is caused by higher $\partial U/\partial y$ and $\partial U/\partial x$, as well as the slightly weaker strength of vortical structures in the FPG region. The resulting shallower structure inclinations are also evident in two-point correlations for u'. Consistent with the low outer layer turbulence, x–z plane data within the logarithmic region show that small-scale structures are almost absent in high-speed regions of the FPG boundary layer, as sweeps force outer layer fluid towards the wall.

In both boundary layers, pressure and pressure gradient fluctuations decrease with increasing distance from the wall. The locally normalized σ_p and $\sigma_{\partial p/\partial x}$ are significantly weaker in the FPG boundary layer than those in the ZPG region. However, when scaled by $\langle u'u' \rangle(x, y)$, profiles of $\sigma_{\partial p/\partial x}$ collapse, and the difference between σ_p profiles is greatly reduced. Two-point correlations of pressure show only slight inclination from the vertical direction, consistent with previous findings. Correlations between p' and v' show that $p' > 0$ is likely to be associated with $\partial v'/\partial x > 0$ and vice versa in the ZPG boundary layer, resulting in two horizontally oriented lobes in the $R_{p,v}$ distributions. This trend presumably results from the contribution of $2(\partial U/\partial y)\partial v'/\partial x$ in the integral of the Poisson equation for p'. Significant contribution of $(\partial V/\partial y)\partial v'/\partial y$ results in inclined lobes of $R_{p,v}$ in the FPG case. In both boundary layers, although the 'slow' terms in the Poisson equation are significantly stronger than the 'fast' terms, they do not contribute substantially to $R_{p,v}$.

In both boundary layers, large-scale ($>1.5\delta$) pressure gradient fluctuations at different elevations are highly correlated and have the same phase. Large-scale sweeps are mostly associated with $\partial \widetilde{p'}/\partial x > 0$, as downward moving fluid decelerates. Conversely, a fluid element is more likely to accelerate as it moves away from the wall. As a result, $\partial \widetilde{p'}/\partial x < 0$ is preferentially associated with large-scale ejections. Similar trends have been reported before, based on experimental wall pressure measurements (e.g. Morrison & Bradshaw 1991) and numerical simulations (e.g. Kim 1983). The observed correlations between $\partial \widetilde{p'}/\partial x$ and $(\widetilde{u'}, \widetilde{v'})$ hold only at corresponding scales of motion. Accordingly, $(\widehat{u'}, \widehat{v'})$ do not show preferred quadrants when $\partial \widetilde{p'}/\partial x$ is positive or negative.

Conditional sampling shows that the sweeping flow structure during periods of $\partial \widetilde{p'}/\partial x > \sigma_{\partial \widetilde{p}/\partial x}$ and $\widetilde{u'} > 0$ is nearly two-dimensional at $y/\delta > 0.1$. However, close to the wall, the flow becomes three-dimensional as the near-wall fluid loses momentum and is stretched in the spanwise direction (splatting flow). In the ZPG boundary layer, the near-wall deceleration causes flow 'separation' (not accounting for the mean flow), which initiates a growing region of ejection and high wall-normal momentum transport underneath the sweep. An inclined, large-scale (3–4δ) shear layer forms at the sweep–ejection interface. Our measurement resolution allows us to detect this phenomenon only after it has grown beyond the buffer layer. Downstream of the 'separation' point, the near-wall flow changes from splatting to anti-splatting, the ejected fluid accelerates as it migrates upward and, accordingly, $\partial\widetilde{p'}/\partial x$ becomes favourable. Even before separation, the near-wall small-scale turbulence increases underneath the sweeps, as the fluid decelerates, and decreases within the ejection region further downstream, as the flow accelerates. The existence of elevated small-scale turbulence underneath regions of high large-scale streamwise velocity fluctuations is consistent with several recent studies (e.g. Hutchins *et al.* 2011). Although significantly weaker than the ZPG case, the correlation between large-scale sweeps and $\partial\widetilde{p'}/\partial x > 0$ persists in the FPG boundary layer. However, since $\sigma_{\partial\widetilde{p}/\partial x} < |\partial P/\partial x|$, the instantaneous large-scale pressure gradient close to the wall rarely becomes positive. As a result, the separation-like phenomenon is weak, and is confined to a very small near-wall domain. The associated small-scale turbulence and momentum transfer do not show elevated levels underneath the sweeps.

In both boundary layers, the flow structure during periods of large-scale ejections and acceleration is again mostly 2D at $y/\delta > 0.2$, but involves near-wall spanwise contraction. The wall-normal momentum flux is substantially higher than $\langle u'v' \rangle$ over a broad area, except very near the wall. In the ZPG boundary layer, the ejections contain numerous familiar trains of rising vortical structures. Conditional sampling and instantaneous realizations confirm that some of the ejections are preceded by regions with sweeps and $\partial\widetilde{p'}/\partial x > 0$, which presumably initiate the ejections. However, some of the ejections are not preceded by sweeps, at least within $\sim 6\delta$ upstream of the $\partial\widetilde{p'}/\partial x < 0$ peak, i.e. other mechanisms must be involved. In the FPG boundary layer, large-scale ejections containing multiple, nearly horizontal trains of vortices are evident during periods of $\partial\widetilde{p'}/\partial x < 0$. Conditional sampling and instantaneous realizations do not show evidence of sweeps or $\partial\widetilde{p'}/\partial x > 0$ within 6δ upstream of the ejections. Evidently, the mechanism involving adverse pressure gradients does not play a significant role in initiation of ejections, implying again that others are more important. The similar un-scaled widths of low-speed regions in the ZPG and FPG boundary layers might indicate that some of these structures propagate all the way from the ZPG domain. Thus, it is still possible that adverse pressure gradients are involved in the initiation of ejections, but the process occurs far upstream of the FPG region.

Acknowledgements

The authors acknowledge the financial support from the National Science Foundation (NSF), initially under grant no. CTS 0625571, and continuing under grant no. CBET 0932941. The pressure measurement technique has been developed with support from the Office of Naval Research (ONR), Ki-Han Kim is the Program Officer. Funding for the high-speed PIV system was provided in part by an ONR DURIP Grant, and in part by an NSF MRI grant. The authors also thank Dr Rinaldo Miorini for help with the time-resolved PIV measurements.

REFERENCES

ADRIAN, R. J. 2007 Hairpin vortex organization in wall turbulence. *Phys. Fluids* **19**, 041301.

ADRIAN, R. J., MEINHART, C. D. & TOMKINS, C. D. 2000 Vortex organization in the outer region of the turbulent boundary layer. *J. Fluid Mech.* **422**, 1–54.

BADRI NARAYANAN, M. A. & RAMJEE, V. 1969 On the criteria for reverse transition in a two-dimensional boundary layer flow. *J. Fluid Mech.* **35** (part 2), 225–241.

BAILEY, S. C. C. & SMITS, A. J. 2010 Experimental investigation of the structure of large- and very-large-scale motions in turbulent pipe flow. *J. Fluid Mech.* **651**, 339–356.

BALAKUMAR, B. J. & ADRIAN, R. J. 2007 Large- and very-large-scale motions in channel and boundary-layer flows. *Phil. Trans. R. Soc.* A **365** (1852), 665–681.

BLACKWELDER, R. F. & KOVASZNAY, L. S. G. 1972 Large-scale motion of a turbulent boundary layer during relaminarization. *J. Fluid Mech.* **53** (part 1), 61–83.

BOURASSA, C. & THOMAS, F. O. 2009 An experimental investigation of a highly accelerated turbulent boundary layer. *J. Fluid Mech.* **634**, 359–404.

BULL, M. K. 1967 Wall-pressure fluctuations associated with subsonic turbulent boundary layer flow. *J. Fluid Mech.* **28** (part 4), 719–754.

CHEN, J., MENEVEAU, C. & KATZ, J. 2006 Scale interactions of turbulence subjected to a straining–relaxation–destraining cycle. *J. Fluid Mech.* **562**, 123–150.

CHOI, H. & MOIN, P. 1990 On the space–time characteristics of wall-pressure fluctuations. *Phys. Fluids* A **2**, 1450–1460.

CHRISTENSEN, K. T. & ADRIAN, R. J. 2002 The velocity and acceleration signatures of small-scale vortices in turbulent channel flow. *J. Turbul.* **3**, N23, 1–28.

CHUNG, D. & MCKEON, B. J. 2010 Large-eddy simulation of large-scale structures in long channel flow. *J. Fluid Mech.* **661**, 341–364.

DE KAT, R. & VAN OUDHEUSDEN, B. W. 2012 Instantaneous planar pressure determination from PIV in turbulent flow. *Exp. Fluids* **52**, 1089–1106.

DEL ÁLAMO, J. C. & JIMÉNEZ, J. 2006 Linear energy amplification in turbulent channels. *J. Fluid Mech.* **559**, 205–213.

DIXIT, S. A. & RAMESH, O. N. 2008 Pressure-gradient-dependent logarithmic laws in sink flow turbulent boundary layers. *J. Fluid Mech.* **615**, 445–475.

DIXIT, S. A. & RAMESH, O. N. 2010 Large-scale structures in turbulent and reverse-transitional sink flow boundary layers. *J. Fluid Mech.* **649**, 233–273.

ELLIOTT, J. A. 1972 Microscale pressure fluctuations measured within the lower atmospheric boundary layer. *J. Fluid Mech.* **53** (part 2), 351–383.

ESCUDIER, M. P., ABDEL-HAMEED, A., JOHNSON, M. W. & SUTCLIFFE, C. J. 1998 Laminarisation and re-transition of a turbulent boundary layer subjected to favourable pressure gradient. *Exp. Fluids* **25**, 491–502.

FERNHOLZ, H. H. & FINLEY, P. J. 1996 The incompressible zero-pressure-gradient turbulent boundary layer: an assessment of the data. *Prog. Aerosp. Sci.* **32**, 245–311.

FERNHOLZ, H. H. & WARNACK, D. 1998 The effects of a favourable pressure gradient and of the Reynolds number on an incompressible axisymmetric turbulent boundary layer. Part 1. The turbulent boundary layer. *J. Fluid Mech.* **359**, 329–356.

GAD-EL-HAK, M. & BANDYOPADHYAY, P. R. 1994 Reynolds number effects in wall-bounded turbulent flows. *Appl. Mech. Rev.* **47** (8), 307–365.

GANAPATHISUBRAMANI, B., HUTCHINS, N., HAMBLETON, W. T., LONGMIRE, E. K. & MARUSIC, I. 2005 Investigation of large-scale coherence in a turbulent boundary layer using two-point correlations. *J. Fluid Mech.* **524**, 57–80.

GANAPATHISUBRAMANI, B., HUTCHINS, N., MONTY, J. P., CHUNG, D. & MARUSIC, I. 2012 Amplitude and frequency modulation in wall turbulence. *J. Fluid Mech.* **712**, 61–91.

GANAPATHISUBRAMANI, B., LONGMIRE, E. K. & MARUSIC, I. 2003 Characteristics of vortex packets in turbulent boundary layers. *J. Fluid Mech.* **478**, 35–46.

GHAEMI, S., RAGNI, D. & SCARANO, F. 2012 PIV-based pressure fluctuations in the turbulent boundary layer. *Exp. Fluids* **53**, 1823–1840.

GUALA, M., METZGER, M. & MCKEON, B. J. 2011 Interactions within the turbulent boundary layer at high Reynolds number. *J. Fluid Mech.* **666**, 573–604.

HARUN, Z., MONTY, J. P., MATHIS, R. & MARUSIC, I. 2013 Pressure gradient effects on the large-scale structure of turbulent boundary layers. *J. Fluid Mech.* **715**, 477–498.

HONG, J., KATZ, J., MENEVEAU, C. & SCHULTZ, M. P. 2012 Coherent structures and associated subgrid-scale energy transfer in a rough-wall turbulent channel flow. *J. Fluid Mech.* **712**, 92–128.

HONG, J., KATZ, J. & SCHULTZ, M. P. 2011 Near-wall turbulence statistics and flow structures over three-dimensional roughness in a turbulent channel flow. *J. Fluid Mech.* **667**, 1–37.

HUNT, J. C. R. & MORRISON, J. F. 2000 Eddy structure in turbulent boundary layers. *Eur. J. Mech. (*B*/Fluids)* **19**, 673–694.

HUTCHINS, N., HAMBLETON, W. T. & MARUSIC, I. 2005 Inclined cross-stream stereo particle image velocimetry measurements in turbulent boundary layers. *J. Fluid Mech.* **541**, 21–54.

HUTCHINS, N. & MARUSIC, I. 2007 Evidence of very long meandering features in the logarithmic region of turbulent boundary layers. *J. Fluid Mech.* **579**, 1–28.

HUTCHINS, N., MONTY, J. P., GANAPATHISUBRAMANI, B., NG, H. C. H. & MARUSIC, I. 2011 Three-dimensional conditional structure of a high-Reynolds-number turbulent boundary layer. *J. Fluid Mech.* **673**, 255–285.

ICHIMIYA, M., NAKAMURA, I. & YAMASHITA, S. 1998 Properties of a relaminarizing turbulent boundary layer under a favourable pressure gradient. *Exp. Therm. Fluid Sci.* **17**, 37–48.

JANG, S. J., SUNG, H. J. & KROGSTAD, P. 2011 Effects of an axisymmetric contraction on a turbulent pipe flow. *J. Fluid Mech.* **687**, 376–403.

JIMÉNEZ, J. & HOYAS, S. 2008 Turbulent fluctuations above the buffer layer of wall-bounded flows. *J. Fluid Mech.* **611**, 215–236.

JIMÉNEZ, J. & PINELLI, A. 1999 The autonomous cycle of near-wall turbulence. *J. Fluid Mech.* **389**, 335–359.

JOHANSSON, A. V., ALFREDSSON, P. H. & KIM, J. 1991 Evolution and dynamics of shear-layer structures in near-wall turbulence. *J. Fluid Mech.* **224**, 579–599.

JONES, W. P. & LAUNDER, B. E. 1972 Some properties of sink-flow turbulent boundary layers. *J. Fluid Mech.* **56** (part 2), 337–351.

JONES, M. B., MARUSIC, I. & PERRY, A. E. 2001 Evolution and structure of sink-flow turbulent boundary layers. *J. Fluid Mech.* **428**, 1–27.

KATZ, J. & SHENG, J. 2010 Applications of holography in fluid mechanics and particle dynamics. *Annu. Rev. Fluid Mech.* **42**, 531–555.

KIM, J. 1983 On the structure of wall-bounded turbulent flows. *Phys. Fluids* **26**, 2088–2097.

KIM, J. 1985 Turbulence structures associated with the bursting event. *Phys. Fluids* **28**, 52–58.

KIM, J. 1989 On the structure of pressure fluctuations in simulated turbulent channel flow. *J. Fluid Mech.* **205**, 421–451.

KIM, K. C. & ADRIAN, R. J. 1999 Very large-scale motion in the outer layer. *Phys. Fluids* **11**, 417–422.

KLINE, S. J., REYNOLDS, W. C., SCHRAUB, F. A. & RUNSTADLER, P. W. 1967 The structure of turbulent boundary layers. *J. Fluid Mech.* **30** (part 4), 741–773.

KOBASHI, Y. & ICHIJO, M. 1986 Wall pressure and its relation to turbulent structure of a boundary layer. *Exp. Fluids* **4**, 49–55.

LENAERS, P., LI, Q., BRETHOUWER, G., SCHLATTER, P. & ÖRLÜ, R. 2012 Rare backflow and extreme wall-normal velocity fluctuations in near-wall turbulence. *Phys. Fluids* **24**, 035110.

LIGRANI, P. M. & MOFFAT, R. J. 1986 Structure of transitionally rough and fully rough turbulent boundary layers. *J. Fluid Mech.* **162**, 69–98.

LIU, Z., ADRIAN, R. J. & HANRATTY, T. J. 2001 Large-scale modes of turbulent channel flow: transport and structure. *J. Fluid Mech.* **448**, 53–80.

LIU, X. & KATZ, J. 2006 Instantaneous pressure and material acceleration measurements using a four-exposure PIV system. *Exp. Fluids* **41**, 227–240.

LIU, X. & KATZ, J. 2013 Vortex–corner interactions in a cavity shear layer elucidated by time-resolved measurements of the pressure field. *J. Fluid Mech.* **728**, 417–457.

LIU, S., KATZ, J. & MENEVEAU, C. 1999 Evolution and modelling of subgrid scales during rapid straining of turbulence. *J. Fluid Mech.* **387**, 281–320.

LO, S. H., VOKE, P. R. & ROCKLIFF, N. J. 2000 Eddy structures in a simulated low Reynolds number turbulent boundary layer. *Flow Turbul. Combust.* **64**, 1–28.

LOZANO-DURÁN, A., FLORES, O. & JIMÉNEZ, J. 2012 The three-dimensional structure of momentum transfer in turbulent channels. *J. Fluid Mech.* **694**, 100–130.

MARUSIC, I., MCKEON, B. J., MONKEWITZ, P. A., NAGIB, H. M., SMITS, A. J. & SREENIVASAN, K. R. 2010 Wall-bounded turbulent flows at high Reynolds numbers: recent advances and key issues. *Phys. Fluids* **22**, 065103.

MATHIS, R., HUTCHINS, N. & MARUSIC, I. 2009 Large-scale amplitude modulation of the small-scale structures in turbulent boundary layers. *J. Fluid Mech.* **628**, 311–337.

MOIN, P. & KIM, J. 1982 Numerical investigation of turbulent channel flow. *J. Fluid Mech.* **118**, 341–377.

MORRISON, J. F. & BRADSHAW, P. 1991 Bursts and sources of pressure fluctuation in turbulent boundary layers. *Eighth Symposium on Turbulent Shear Flows, Technical University of Munich, September 9–11, 1991 Paper 2-1*.

NATRAJAN, V. K., WU, Y. & CHRISTENSEN, K. T. 2007 Spatial signatures of retrograde spanwise vortices in wall turbulence. *J. Fluid Mech.* **574**, 155–167.

PANTON, R. L. 2001 Overview of the self-sustaining mechanisms of wall turbulence. *Prog. Aerosp. Sci.* **37**, 341–383.

PANTON, R. L., GOLDMAN, A. L., LOWERY, R. L. & REISCHMAN, M. M. 1980 Low-frequency pressure fluctuations in axisymmetric turbulent boundary layers. *J. Fluid Mech.* **97** (part 2), 299–319.

PATEL, V. C. & HEAD, M. R. 1968 Reversion of turbulent to laminar flow. *J. Fluid Mech.* **34** (part 2), 371–392.

PEARCE, N. F., DENISSENKO, P. & LOCKERBY, D. A. 2013 An experimental study into the effects of streamwise and spanwise acceleration in a turbulent boundary layer. *Exp. Fluids* **54** (1), 1–17.

PIOMELLI, U., BALARAS, E. & PASCARELLI, A. 2000 Turbulent structures in accelerating boundary layers. *J. Turbul.* **1**, N1, 1–16.

POPE, S. B. 2000 *Turbulent Flows*. Cambridge University Press.

RAFFEL, M., WILLERT, C. E., WERELEY, S. T. & KOMPENHANS, J. 2007 *Particle Image Velocimetry: A Practical Guide*. Springer.

ROBINSON, S. K. 1991 Coherent motions in the turbulent boundary layer. *Annu. Rev. Fluid Mech.* **23**, 601–639.

ROTH, G. I. & KATZ, J. 2001 Five techniques for increasing the speed and accuracy of PIV interrogation. *Meas. Sci. Technol.* **12**, 238–245.

SCHOLS, J. L. J. & WARTENA, L. 1986 A dynamical description of turbulent structures in the near neutral atmospheric surface layer: the role of static pressure fluctuations. *Boundary-Layer Meteorol.* **34**, 1–15.

SCHOPPA, W. & HUSSAIN, F. 2002 Coherent structure generation in near-wall turbulence. *J. Fluid Mech.* **453**, 57–108.

SHAH, M. K., AGELINCHAAB, M. & TACHIE, M. F. 2008 Influence of PIV interrogation area on turbulent statistics up to 4th order moments in smooth and rough wall turbulent flows. *Exp. Therm. Fluid Sci.* **32** (3), 725–747.

SHENG, J., MALKIEL, E. & KATZ, J. 2008 Using digital holographic microscopy for simultaneous measurements of 3D near wall velocity and wall shear stress in a turbulent boundary layer. *Exp. Fluids* **45**, 1023–1035.

SHENG, J., MALKIEL, E. & KATZ, J. 2009 Buffer layer structures associated with extreme wall stress events in a smooth wall turbulent boundary layer. *J. Fluid Mech.* **633**, 17–60.

SMITH, C. R., WALKER, J. D. A., HAIDARI, A. H. & SOBRUN, U. 1991 On the dynamics of near-wall turbulence. *Phil. Trans.* **336** (1641), 131–175.

SPALART, P. R. 1986 Numerical study of sink-flow boundary layers. *J. Fluid Mech.* **172**, 307–328.

SPALART, P. R. 1988 Direct simulation of a turbulent boundary layer up to $R_\theta = 1410$. *J. Fluid Mech.* **187**, 61–98.

SREENIVASAN, K. R. 1982 Laminarescent, relaminarizing and retransitional flows. *Acta Mechanica* **44**, 1–48.

TALAMELLI, A., FORNACIARI, N., JOHAN, K., WESTIN, K. J. A. & ALFREDSSON, P. H. 2002 Experimental investigation of streaky structures in a relaminarizing boundary layer. *J. Turbul.* **3**, N18, 1–13.

TALAPATRA, S. & KATZ, J. 2012 Coherent structures in the inner part of a rough-wall channel flow resolved using holographic PIV. *J. Fluid Mech.* **711**, 161–170.

TALAPATRA, S. & KATZ, J. 2013 Three-dimensional velocity measurements in a roughness sublayer using microscopic digital in-line holography and optical index matching. *Meas. Sci. Technol.* **24**, 024004.

THOMAS, A. S. W. & BULL, M. K. 1983 On the role of wall-pressure fluctuations in deterministic motions in the turbulent boundary layer. *J. Fluid Mech.* **128**, 283–322.

TOH, S. & ITANO, T. 2005 Interaction between a large-scale structure and near-wall structures in channel flow. *J. Fluid Mech.* **524**, 249–262.

TOMKINS, C. D. & ADRIAN, R. J. 2003 Spanwise structure and scale growth in turbulent boundary layers. *J. Fluid Mech.* **490**, 37–74.

TOWNSEND, A. A. 1976 *The Structure of Turbulent Shear Flow*. Cambridge University Press.

TSUJI, Y., FRANSSON, J. H. M., ALFREDSSON, P. H. & JOHANSSON, A. V. 2007 Pressure statistics and their scaling in high-Reynolds-number turbulent boundary layers. *J. Fluid Mech.* **585**, 1–40.

TSUJI, Y., IMAYAMA, S., SCHLATTER, P., ALFREDSSON, P. H., JOHANSSON, A. V., MARUSIC, I., HUTCHINS, N. & MONTY, J. 2012 Pressure fluctuation in high-Reynolds-number turbulent boundary layer: results from experiments and DNS. *J. Turbul.* **13**, N50, 1–19.

TUTKUN, M., GEORGE, W. K., DELVILLE, J., STANISLAS, M., JOHANSSON, P. B. V., FOUCAUT, J. -M. & COUDERT, S. 2009 Two-point correlations in high Reynolds number flat plate turbulent boundary layers. *J. Turbul.* **10**, N21, 1–23.

WILLMARTH, W. W. & WOOLDRIDGE, C. E. 1962 Measurements of the fluctuating pressure at the wall beneath a thick turbulent boundary layer. *J. Fluid Mech.* **14** (2), 187–210.

WILLS, J. A. B. 1970 Measurements of the wavenumber/phase velocity spectrum of wall pressure beneath a turbulent boundary layer. *J. Fluid Mech.* **45** (part 1), 65–90.

WU, Y. & CHRISTENSEN, K. T. 2006 Population trends of spanwise vortices in wall turbulence. *J. Fluid Mech.* **568**, 55–76.

WU, H., MIORINI, R. L. & KATZ, J. 2011 Measurements of the tip leakage vortex structures and turbulence in the meridional plane of an axial water-jet pump. *Exp. Fluids* **50**, 989–1003.

ZHOU, J., ADRIAN, R. J. & BALACHANDAR, S. 1996 Autogeneration of near-wall vortical structures in channel flow. *Phys. Fluids* **8**, 288–290.

ZHOU, J., ADRIAN, R. J., BALACHANDAR, S. & KENDALL, T. M. 1999 Mechanisms for generating coherent packets of hairpin vortices in channel flow. *J. Fluid Mech.* **387**, 353–396.